

1 **Augmentation of WRF-Hydro to Simulate Overland Flow- and**  
2 **Streamflow-Generated Debris Flow Susceptibility in Burn Scars**

3  
4 **Chuxuan Li<sup>1</sup>, Alexander L. Handwerker<sup>2,3</sup>, Jiali Wang<sup>4</sup>, Wei Yu<sup>5,6</sup>, Xiang Li<sup>7</sup>, Noah J.**  
5 **Finnegan<sup>8</sup>, Yingying Xie<sup>9,10</sup>, Giuseppe Buscarnera<sup>7</sup>, and Daniel E. Horton<sup>1</sup>**

6 <sup>1</sup> Department of Earth and Planetary Sciences, Northwestern University, Evanston, IL, 60208, USA

7 <sup>2</sup> Joint Institute for Regional Earth System Science and Engineering, University of California, Los Angeles,  
8 CA, 90095, USA

9 <sup>3</sup> Jet Propulsion Laboratory, California Institute of Technology, Pasadena, CA, 91109, USA

10 <sup>4</sup> Environmental Science Division, Argonne National Laboratory, Lemont, IL, 60439, USA

11 <sup>5</sup> Cooperative Institute for Research in Environmental Sciences, University of Colorado Boulder, CO,  
12 80309, USA

13 <sup>6</sup> NOAA/Global Systems Laboratory, 325 Broadway Boulder, Denver, CO, 80305-3328, USA

14 <sup>7</sup> Department of Civil and Environmental Engineering, Northwestern University, Evanston, IL, 60208, USA

15 <sup>8</sup> Department of Earth and Planetary Sciences, University of California Santa Cruz, Santa Cruz, CA, 95064,  
16 USA

17 <sup>9</sup> Program in Environmental Sciences, Northwestern University, 2145 Sheridan Road, Evanston, IL, 60208,  
18 USA

19 <sup>10</sup> Department of Biological Sciences, Purdue University, 915 W State St, West Lafayette, IN 47907, USA

20  
21 *Correspondence to:* Chuxuan Li ([chuxuanli2020@u.northwestern.edu](mailto:chuxuanli2020@u.northwestern.edu))

29 **Abstract**

30 In steep wildfire-burned terrains, intense rainfall can produce large volumes of runoff that can  
31 trigger highly destructive debris flows. However, the ability to accurately characterize and forecast  
32 debris-flow susceptibility in burned terrains using physics-based tools remains limited. Here, we  
33 augment the Weather Research and Forecasting Hydrological modeling system (WRF-Hydro) to  
34 simulate both overland and channelized flows and assess postfire debris flow susceptibility over a  
35 regional domain. We perform hindcast simulations using high-resolution weather radar-derived  
36 precipitation and reanalysis data to drive non-burned baseline and burn scar sensitivity  
37 experiments. Our simulations focus on January 2021 when an atmospheric river triggered  
38 numerous debris flows within a wildfire burn scar in Big Sur – one of which destroyed California’s  
39 famous Highway 1. Compared to the baseline, our burn scar simulation yields dramatic increases  
40 in total and peak discharge, and shorter lags between rainfall onset and peak discharge, consistent  
41 with streamflow observations at nearby U.S. Geological Survey (USGS) streamflow gage sites.  
42 For the 404 catchments located in the simulated burn scar area, median catchment-area normalized  
43 discharge volume increases nine-fold compared to the baseline. Catchments with anomalously  
44 high catchment-area normalized discharge volumes correspond well with post-event field-based  
45 and remotely-sensed debris flow observations. We suggest that our regional post-fire debris flow  
46 susceptibility analysis demonstrates WRF-Hydro as a compelling new physics-based tool whose  
47 utility could be further extended via coupling to sediment erosion and transport models and/or  
48 ensemble-based operational weather forecasts. Given the high-fidelity performance of our  
49 augmented version of WRF-Hydro, as well as its potential usage in probabilistic hazard forecasts,  
50 we argue for its continued development and application in post-fire hydrologic and natural hazard  
51 assessments.

52

53 **Short Summary**

54 In January 2021 a storm triggered numerous debris flows in a wildfire burn scar, California. We  
55 use a hydrologic model to assess debris flow susceptibility in pre-fire and postfire scenarios.  
56 Compared to pre-fire conditions, postfire simulation yields dramatic increases in total and peak  
57 discharge, substantially increasing debris flow susceptibility. Our work proves the 3-D hydrologic  
58 models' utility to investigate and potentially forecast postfire debris flow susceptibility at regional  
59 scales.

60 **1 Introduction**

61 Following intense rainfall, areas with wildfire burn scars are more prone to flash flooding (Neary  
62 et al., 2003; Bart & Hope 2010; Bart 2016) and runoff-generated debris flows than unburned areas  
63 (Ice et al., 2004; Shakesby & Doerr, 2006; Moody et al., 2013). After wildfire, reduced tree canopy  
64 interception, decreased soil infiltration due to soil-sealing effects (Larsen et al., 2009), and

65 increased soil water repellency – especially in hyper-arid environments (Dekker & Ritsema, 1994;  
66 Doerr & Thomas, 2000; MacDonald & Huffman, 2004) – increases excess surface water, and on  
67 sloped terrains leads to overland flow (Shakesby & Doerr, 2006; Stoof et al., 2012). As water  
68 moves down hillslopes and erosion adds sediment to water-dominated flows, clear water floods  
69 can transition to turbulent and potentially destructive debris flows (Meyer & Wells, 1997; Cannon  
70 et al., 2001, 2003; Santi et al., 2008). In contrast to debris flows initiated by shallow landslides,  
71 this rainfall-runoff process has been identified as the major cause for postfire debris flows in the  
72 western U.S. (Cannon, 2001; Cannon et al., 2003, 2008; Kean et al., 2011; Parise & Cannon, 2012;  
73 Nyman et al., 2015), and in other regions with Mediterranean climates (Bisson et al., 2005;  
74 Mitsopoulos & Mironidis, 2006; Rosso et al., 2007; Parise & Cannon, 2008, 2009). In California,  
75 because climate change is projected to increase the intensity and frequency of wet-season  
76 precipitation (Polade et al., 2017; Swain et al., 2018), increase wildfire potential (Brown et al.,  
77 2020; Swain, 2021), and extend the wildfire season (Goss et al., 2020), occurrence and intensity  
78 of postfire debris flows are likely to increase (Cannon & DeGraff, 2009; Kean & Staley, 2021;  
79 Oakley, 2021).

80 Due to this increasing threat, the development of tools to assess postfire debris flow susceptibility  
81 and hazards is critical. However, due to long-standing terminology ambiguity in the natural hazard  
82 community (Reichenbach et al., 2018), we first begin with a definition of terms. In this study we  
83 demonstrate the use of a new physics-based tool to map postfire debris flow susceptibility at  
84 regional scales. We follow the guidance of [Reichenbach et al., (2018) & references therein] and  
85 define *susceptibility* as the likelihood of debris flow occurrence in an area, and *hazard* as the  
86 probability of debris flow occurrence of a given magnitude within a specified area and period of  
87 time. In other words, debris flow susceptibility does not estimate debris flow size or consider the  
88 timing or frequency of the debris flow occurrence. Rather, it focuses on locating areas prone to  
89 debris flows considering local environmental factors (Brabb 1985; Guzzetti et al., 2005).

90 Heuristic, deterministic, statistical approaches, and coupled deterministic and statistical models  
91 have previously been employed to assess landslide susceptibility (Dahal et al., 2008; Regmi et al.,  
92 2010; Park et al., 2016; Reichenbach et al., 2018). For postfire debris flow susceptibility or hazard  
93 assessment, however, the use of deterministic models is limited. In contrast, statistical approaches  
94 are commonly used in both research and operational settings (Cannon et al., 2010; Friedel 2011a,  
95 2011b; Gardner et al., 2014; Staley et al., 2016; Nikolopoulos et al., 2018; Cui et al., 2019). For  
96 example, rainfall intensity-duration (ID) thresholds are one of the simplest-to-implement and most  
97 widely used statistical methods for mapping rainfall-induced landslide susceptibility including  
98 postfire debris flows (Cannon et al., 2011; Staley et al., 2017). In addition, the U.S. Geological  
99 Survey (USGS) currently employs a statistical approach in their Emergency Assessment of  
100 Postfire Debris-flow Hazards that consists of a logistic regression model to predict the likelihood  
101 of post-wildfire debris flows (e.g., Cannon et al., 2010; Staley et al., 2016), and a multiple linear  
102 regression model to predict debris flow volumes (Gartner et al., 2014). Machine-learning  
103 techniques such as self-organizing maps, genetic programming, and a random forest algorithm  
104 have also been used to predict postfire debris flows in the western U.S. (Friedel 2011a, 2011b;

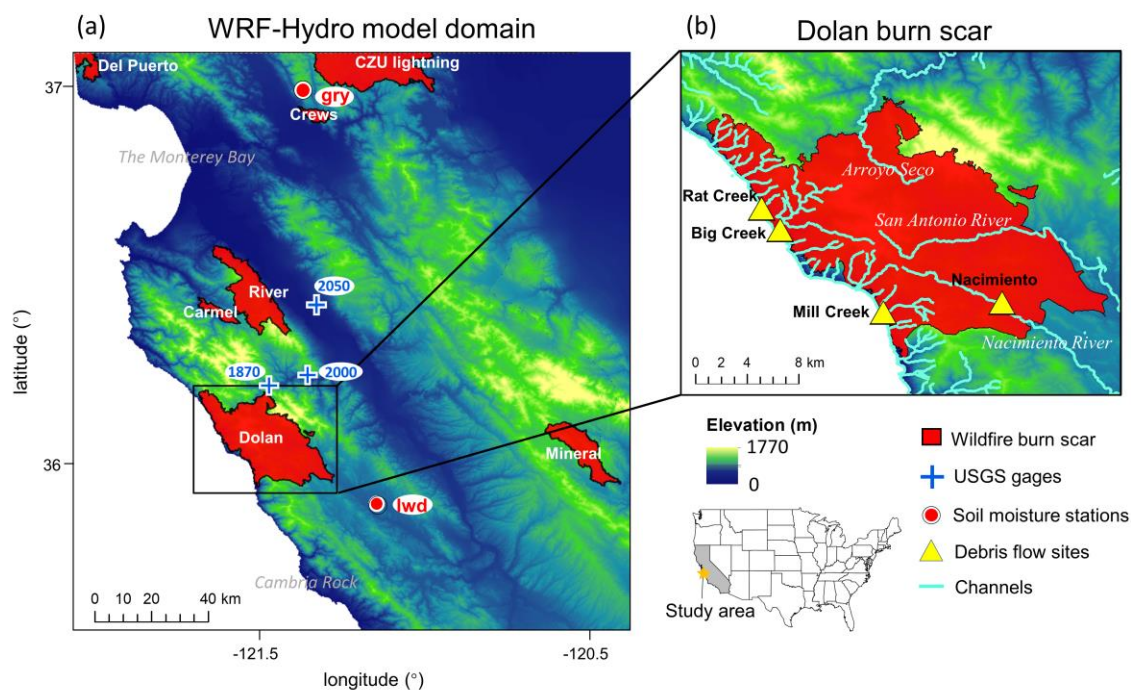
105 Nikolopoulos et al., 2018). In general, statistical approaches are useful for identifying and  
106 characterizing relationships amongst contributing environmental factors and are widely used due  
107 to their low computational costs and the potential for rapid assessment. Despite the utility and  
108 advantages of data-driven hazard prediction approaches over regional domains, these techniques  
109 (1) do not simulate the underlying physics, (2) often require large amount of historical observation  
110 data that may not be readily available, and (3) result in models that are often only applicable to  
111 specific locales. These limitations inhibit their utility in developing a better process-based  
112 understanding of debris flow mechanics, limit their applicability in climatological and geographic  
113 settings different than their training sites, and limit their use in non-stationary conditions (e.g.,  
114 under changing climatic conditions).

115 In contrast, physics-based models that simulate spatially-explicit hydrologic and mass wastage  
116 processes are well-suited for mechanistic sensitivity analyses in diverse settings. However, studies  
117 employing deterministic process-based models have tended to focus on modeling rainfall-induced  
118 shallow landslides (Crosta & Frattini, 2003; Claessens et al., 2007) or landslide-induced debris  
119 flows (e.g., Iverson & George, 2014; George & Iverson, 2014), rather than on runoff-generated  
120 debris flows which are more common in postfire areas (Cannon et al., 2001, 2003; Santi et al.,  
121 2008). Studies that have investigated postfire hydrologic responses using physics-based models  
122 have largely focused on short-term responses at high spatiotemporal resolutions (Rengers et al.,  
123 2016; McGuire et al., 2016, 2017) or long-term runoff responses at coarse temporal resolutions  
124 (McMichael & Hope, 2007; Rulli & Rosso, 2007) in individual catchments rather than assessing  
125 susceptibility over regional domains. For example, process-based models have employed shallow  
126 water equations to understand the triggering and transport mechanisms of postfire debris flows in  
127 single catchments (McGuire et al., 2016, 2017) and to investigate the timing of postfire debris  
128 flows in three separate catchments (Rengers et al., 2016), the latter of which also assessed the  
129 efficacy of a simplified kinematic wave approach. In addition to individual catchment applications,  
130 process-based models often adopt simplifications that can limit effective prediction and hypothesis  
131 testing to overcome computational limits. For example, the kinematic runoff and erosion model  
132 (KINEROS2) simplifies drainage basins into 1-dimensional channels and hillslope patches  
133 (Canfield et al., 2005; Goodrich et al., 2012; Sidman et al., 2016), and the Hydrologic Modeling  
134 System (HEC-HMS) uses an empirically-based curve number method to estimate saturation excess  
135 water (Cydzik et al., 2009), which cannot resolve infiltration excess overland flow, a critical  
136 process in burn scars (Chen et al., 2013).

137 Given the current state of debris flow susceptibility assessment and prediction in previously burned  
138 terrains, in addition to the growing influence of anthropogenic climate change on wildfire and  
139 extreme precipitation, development of physics-based susceptibility mapping tools that can be used  
140 in both hindcast investigations and forecasting applications is needed. Furthermore, due to the  
141 diverse morphology and often large spatial scales of precipitation events and their interactions with  
142 geographically distributed wildfire burn scars, development of tools that can assess susceptibility  
143 over regional domains, particularly in operational forecasting applications, is critical. Here, to  
144 advance the field of burn scar debris flow susceptibility assessment, we explore the use of the

145 physics-based and fully-distributed Weather Research and Forecasting Hydrological modeling  
146 system version 5.1.1 (WRF-Hydro). WRF-Hydro is an open-source community model developed  
147 by the National Center for Atmospheric Research (NCAR). It is the core of the National Oceanic  
148 and Atmospheric Administration's (NOAA) National Water Model forecasting system and has  
149 been used extensively to study channelized flows over regional domains (e.g., Wang et al., 2019;  
150 Lahmers et al., 2020). Here, we modify WRF-Hydro to output high temporal resolution fine-scale  
151 (100 m) debris flow-relevant overland flow; a process computed using a fully unsteady, explicit,  
152 finite difference diffusive wave formulation. Previous efforts, employing shallow water equations,  
153 diffusive, kinematic, and diffusive-kinematic wave models, have demonstrated that water-only  
154 models can provide critical insights on runoff-driven debris flow behavior (Arattano & Savage,  
155 1994; Arratano & Franzi, 2010; Di Cristo et al., 2021), even in burned watersheds (Rengers et al.,  
156 2016; McGuire & Youberg, 2020).

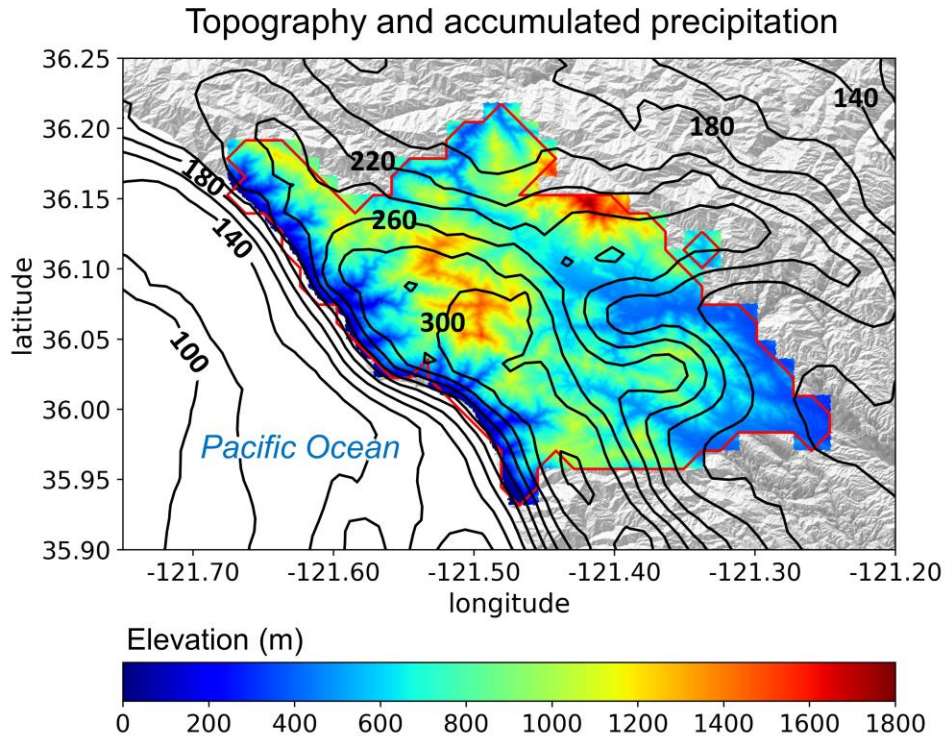
157 To test and demonstrate the utility of WRF-Hydro in debris flow studies, we investigate the  
158 January 2021 debris flow events within the Dolan burn scar on the Big Sur coast of central  
159 California (Fig. 1a–b). We first identify multiple debris flow sites using optical and radar remote  
160 sensing data and field investigations. We then calibrate WRF-Hydro against ground-based soil  
161 moisture and streamflow observations and use it to study the effects of burn scars on debris flow  
162 hydrology and susceptibility. The paper is organized as follows. Section 2 describes the  
163 identification approach and geologic setting of debris flows. Section 3 presents a description of  
164 WRF-Hydro. Section 4 describes the simulation, calibration, and validation of WRF-Hydro.  
165 Section 5 presents the results. Section 6 discusses the results and Sect. 7 provides a conclusion.



166  
 167 **Fig. 1|** WRF-Hydro model domain and Dolan burn scar. (a) WRF-Hydro model domain depicting  
 168 topography, 2020 wildfire season burn scars, and PSL soil moisture and USGS stream gage  
 169 observing sites. The black rectangle outlines (b) the Dolan burn scar inset, in which debris flow  
 170 locations and major streams are marked and labeled. The location of the study area is shown in the  
 171 embedded U.S. map with the state of California shaded in grey.

172  
 173 **2 Study domain and debris flow identification methodology**

174 The Dolan wildfire burned from August 18<sup>th</sup> till December 31<sup>st</sup>, 2020. 55% of areas within the fire  
 175 perimeter were burned at moderate-to-high severity (Burned Area Emergency Response, 2020).  
 176 After the fire, USGS Emergency Assessment of Postfire Debris-flow Hazards produced a debris  
 177 flow hazard assessment using a design storm based statistical model (USGS, 2020). On January  
 178 27–29, 2021, an atmospheric river (AR) made landfall on the Big Sur coast, bringing more than  
 179 300 mm of rainfall to California’s Coast Ranges (Fig. 2), with a peak rainfall rate of 24 mm h<sup>-1</sup>.  
 180 During the AR event, a section of California State Highway 1 (CA1) at Rat Creek was destroyed  
 181 by a debris flow. CA1 was subsequently closed for three months and rebuilt at a cost of ~\$11.5M  
 182 (Los Angeles Times, 2021).



184  
185  
186  
187  
188  
189  
190  
191

**Fig. 2|** The topography (shading; m) and MRMS accumulated precipitation (contour lines; mm) during the AR event from January 27<sup>th</sup> 00:00 to 29<sup>th</sup> 23:00 in the Dolan burn scar. Contour line interval for accumulated precipitation is 20 mm, and lines of 100, 140, 180, 220, 260, and 300 mm are labeled. The red polygon outlines the perimeter of the Dolan burn scar.

## 192 2.1 Debris flow identification from remote sensing and field work

193 In addition to the Rat Creek debris flow, which made national news (Los Angeles Times, 2021),  
194 we identified three other debris flows using a combination of field investigation, and open access  
195 satellite optical and synthetic aperture radar (SAR) images (Fig. 3 and Fig. B1).

196 We examined relative differences in normalized difference vegetation index (rdNDVI) defined by  
197 (Scheip & Wegmann, 2021):

$$198 \quad rdNDVI = \frac{NDVI_{post} - NDVI_{pre}}{\sqrt{NDVI_{pre} + NDVI_{post}}} \times 100 \quad (1)$$

199 where  $NDVI_{pre}$  and  $NDVI_{post}$  are the pre- and post-event normalized difference vegetation index  
200 (NDVI) images computed following:

$$201 \quad NDVI = \frac{NIR - Red}{NIR + Red} \quad (2)$$

202 where *NIR* is the near-infrared response and *Red* is the visible red response. rdNDVI was calculated  
 203 from Sentinel-2 satellite data using the HazMapper v1.0 Google Earth Engine application (Scheip  
 204 & Wegmann, 2021). HazMapper requires selection of an event date, pre-event window (months),  
 205 post-event window (months), max cloud cover (%) and slope threshold (°). These input  
 206 requirements filter the number of images used to calculate the rdNDVI. We set the event date to  
 207 January 27<sup>th</sup>, 2021 and used a 3 month pre- and post-event window with 0% max cloud cover and  
 208 a 0° slope threshold to identify vegetation loss associated with the debris flows. We then created  
 209 a binary map to highlight debris flows (and other vegetation loss) pixels above a rdNDVI  
 210 vegetation loss threshold. We removed all pixels with rdNDVI > -10.

211 Lastly, we searched for debris flows (and other ground surface deformation) by examining SAR  
 212 backscatter change with data acquired by the Copernicus Sentinel-1 (S1) satellites [see full  
 213 description in Handwerger et al. (2022)]. We measured the change in SAR backscatter by using  
 214 the log ratio approach, defined as

$$215 \quad I_{ratio} = 10 \times \log_{10} \left( \frac{\sigma_{pre}^0}{\sigma_{post}^0} \right) \quad (3)$$

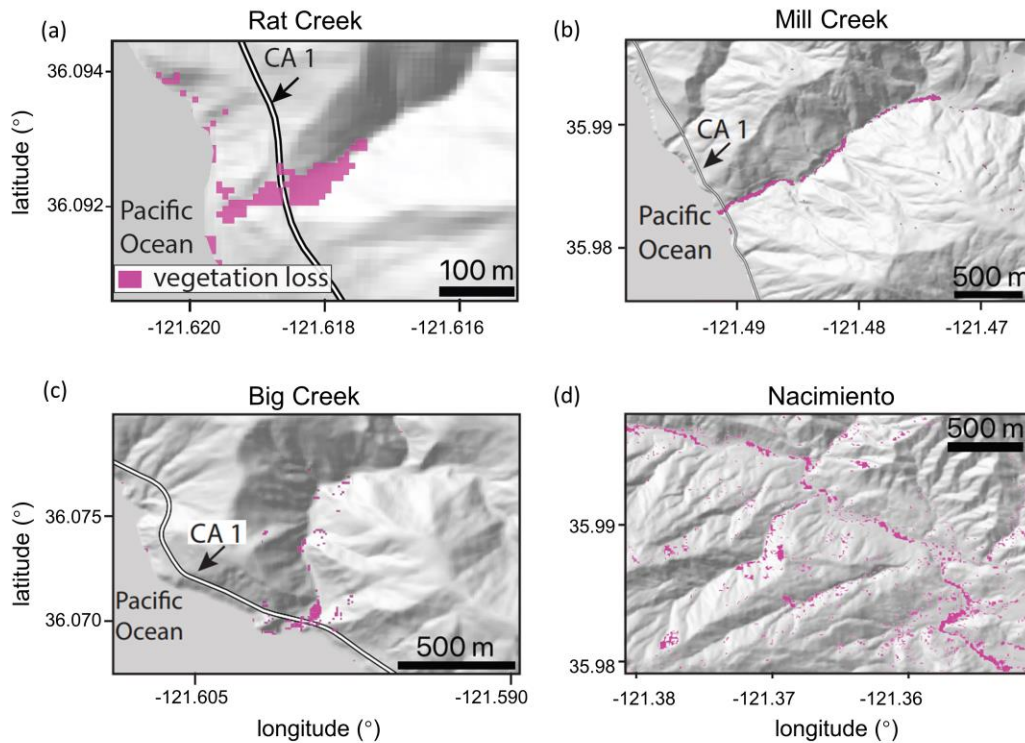
216 where  $\sigma_{pre}^0$  is a pre-event image stack (defined as the temporal median) of SAR backscatter and  
 217  $\sigma_{post}^0$  is a post-event image stack. Similar to the HazMapper method, our approach requires  
 218 selection of an event date, pre-event window (months), post-event window (months) and slope  
 219 threshold (°). No cloud-cover threshold is needed since SAR penetrates clouds. We used a 3 month  
 220 pre- and post-event window and 0° slope threshold to identify ground surface changes associated  
 221 with the debris flows. We then created a binary map to highlight debris flows by removing all  
 222 pixels with  $I_{ratio} < 99^{\text{th}}$  percentile value [i.e., threshold suggested by Handwerger et al. (2022)].

223 Identified debris flow source areas and deposition sites were confirmed by field investigation (N.J.  
 224 Finnegan) and named after the locations where they deposited (i.e., Big Creek, Mill Creek, and  
 225 Nacimiento).

226



## rdNDVI vegetation change



227

228 **Fig. 3]** Identified debris flow sites using rdNDVI vegetation change within the Dolan burn scar.  
229 We convert the rdNDVI data into a binary map by setting a threshold value, which yields only the  
230 likely debris flow locations and drape these maps over a topographic hillshade. (a)–(d) Sentinel-2  
231 rdNDVI vegetation change at (a) Rat Creek, (b) Mill Creek, (c) Big Creek, and (d) the Nacimiento  
232 River.

233

### 234 **2.2 Debris flow geologic setting**

235 According to the USGS National Elevation Dataset 30-m digital elevation model (DEM), the Rat  
236 Creek debris flow sits at the base of a 1<sup>st</sup> order catchment with a drainage area of 2.23 km<sup>2</sup>. Mill  
237 Creek, Big Creek, and Nacimiento debris flows were initiated within extremely steep, intensely  
238 burned, 1<sup>st</sup> order catchments, but were deposited in 2<sup>nd</sup>, 3<sup>rd</sup>, and 3<sup>rd</sup> Strahler stream order channels,  
239 respectively. All four debris flows were channelized. Rat Creek, Mill Creek, and Big Creek debris  
240 flow deposition sites have elevations ranging from 20–60 m, while Nacimiento debris flow  
241 deposited at an elevation of ~440 m above sea level. We calculate catchment slopes using the DEM  
242 and the slope calculation function in ArcMap. The average slope of the catchments containing Rat  
243 Creek and Mill Creek debris flow deposition sites is ~25°. The average catchment slope of Big  
244 Creek deposition site is ~28° and Nacimiento is ~21°. For debris flow source areas, the average

245 and maximum slopes of Mill Creek are 23° and 39°, 21° and 43° for Big Creek, and 24° and 41°  
246 for Nacimiento. According to the Soil Survey Geographic Database and California geologic map  
247 data, surface soils at the three coastal debris flow sites (i.e., Rat Creek, Mill Creek, and Big Creek)  
248 are texturally classified as loam with underlying Franciscan Complex sedimentary rocks of  
249 Jurassic to Cretaceous age. Soil at Nacimiento is classified as sandy loam with underlying Upper  
250 Cretaceous and Paleocene marine sedimentary rocks from the Dip Creek Formation, Asuncion  
251 Group, Shut-In Formation, Italian Flat Formation, Steve Creek Formation, and El Piojo Formation.  
252 Mill Creek, Big Creek, and Nacimiento were relatively large debris flows with runout lengths  
253 between ~2–5 km, while Rat Creek occurred in a smaller catchment and had a runout length of  
254 ~300 m. The difference in runout length and debris flow size is primarily controlled by upstream  
255 catchment size, however for the three coastal debris flow events at Rat Creek, Big Creek, and Mill  
256 Creek, also constrained by the downslope ocean. We note that there were likely more debris flows  
257 triggered during the AR event. The four debris flow events highlighted here were identified during  
258 brief post-event field excursions due to their intersection with major roadways. Given that our  
259 primary goal here is to demonstrate the utility of WRF-Hydro – a comprehensive catalogue of  
260 debris flows is beyond the scope of this study, although underway by other researchers (Cavagnaro  
261 et al., 2021).

## 262 **3 WRF-Hydro**

### 263 **3.1 Model description**

264 WRF-Hydro is an open-source physics-based community model that simulates land surface  
265 hydrologic processes. It includes the Noah-Multiparameterization (Noah-MP) land surface model  
266 (LSM; Niu et al., 2011), terrain routing module, channel routing module, and a conceptual  
267 baseflow bucket model. The Noah-MP LSM is a 1-dimensional column model that calculates  
268 vertical energy fluxes (i.e., sensible and latent heat, net radiation), moisture (i.e., canopy  
269 interception, infiltration, infiltration excess, deep percolation), and soil thermal and moisture states  
270 on the LSM grid (1 km in our application). The infiltration excess, ponded water depth, and soil  
271 moisture are then disaggregated using a time-step weighted method (Gochis & Chen, 2003) and  
272 sent to the terrain routing module which simulates subsurface and overland flows on a finer terrain  
273 routing grid (100 m in our application). According to the mass balance, local infiltration excess,  
274 overland flow, and exfiltration from baseflow contribute to the surface head which flows into river  
275 channels if defined retention depth is exceeded. The channel routing module then calculates  
276 channelized flows assuming a trapezoidal channel shape (Fig. B2). Parameters related to the  
277 trapezoidal channel, such as channel bottom width ( $B_w$ ), Manning’s roughness coefficient ( $n$ ), and  
278 channel side slope ( $z$ ) are functions of channel stream order (Fig. B3 and Table B1). Computed  
279 streamflow is then output on the 100 m grid. Equations used to compute infiltration excess,  
280 overland flow, and channelized flow are provided in Sect. 3.3 and 3.4.

281 By default, WRF-Hydro uses Moderate Resolution Imaging Spectroradiometer (MODIS)  
 282 Modified International Geosphere-Biosphere Program (IGBP) 20-category land cover product as  
 283 land cover (Fig. B4) and 1-km Natural Resources Conservation Service State Soil Geographic  
 284 (STATSGO) database for soil type classification (Fig. B5; Miller & White, 1998). Land surface  
 285 properties including canopy height (HVT), maximum carboxylation rate (VCMX25), and overland  
 286 flow roughness (OV\_ROUGH2D) are functions of land cover type (Table B2 & Fig. B4). Default  
 287 soil hydraulic parameters in WRF-Hydro (i.e., soil porosity, grain size distribution index, and  
 288 saturated hydraulic conductivity) are based on Cosby et al.'s (1984) soil analysis (Table B3) and  
 289 are used to map onto the STATSGO 16 soil texture types (Fig. B5).

290

### 291 **3.2 Meteorological forcing files**

292 WRF-Hydro is used in a standalone mode (i.e., it is not interactively coupled with the atmospheric  
 293 component of WRF), but rather is forced with a combination of Phase 2 North American Land  
 294 Data Assimilation System (NLDAS-2) meteorological data and Multi-Radar/Multi-Sensor System  
 295 (MRMS) radar-only quantitative precipitation (Zhang et al., 2011, 2014, 2016). A description of  
 296 the MRMS dataset and uncertainties therein can be found in Appendix A. NLDAS-2 provides  
 297 hourly forcing data including incoming shortwave and longwave radiation, 2-m specific humidity  
 298 and air temperature, surface pressure, and 10-m wind speed at 1/8-degree spatial resolution.  
 299 MRMS provides hourly precipitation rates at 1-km resolution.

300

### 301 **3.3 Overland flow routing and output**

302 The Noah-MP LSM calculates rate of infiltration excess following Chen & Dudhia (2001):

303

$$304 \quad \frac{\partial h}{\partial t} = \frac{\partial P_d}{\partial t} \left\{ 1 - \frac{[\sum_{i=1}^4 \Delta D_i (\theta_s - \theta_i)] \left[ 1 - \exp \left( -k \frac{K_s}{K_{ref}} \delta_t \right) \right]}{P_d + [\sum_{i=1}^4 \Delta D_i (\theta_s - \theta_i)] \left[ 1 - \exp \left( -k \frac{K_s}{K_{ref}} \delta_t \right) \right]} \right\} \quad (4)$$

305

306 where  $h$  (m) is the surface water depth and  $t$  is the time.  $P_d$  (m) is the precipitation not intercepted  
 307 by the canopy;  $\Delta D_i$  (m) is the depth of soil layer  $i$ ;  $\theta_i$  is the soil moisture in soil layer  $i$ ;  $\theta_s$  is the  
 308 soil porosity;  $K_s$  ( $\text{m s}^{-1}$ ) is the saturated hydraulic conductivity;  $K_{ref}$  is  $2 \times 10^{-6} \text{ m s}^{-1}$  which  
 309 represents the saturated hydraulic conductivity of the silty-clay-loam soil texture chosen as a  
 310 reference;  $\delta_t$  (s) is the model time step; and  $k$  which is equal to 3.0 is the runoff-infiltration  
 311 partitioning parameter [the same as  $kdt_{ref}$  in Chen & Dudhia (2001)].

312

313 Noah-MP passes excess water to the terrain routing module, which simulates overland flow using  
 314 a 2-dimensional fully-unsteady, explicit, finite-difference diffusive wave equation adapted from  
 315 Julien et al. (1995) and Ogden (1997). It is considered improved compared to the traditionally used  
 316 kinematic wave formulation in that it accounts for backwater effects and flow over adverse slopes.  
 317 The diffusive wave formulation is the simplified form of the Saint Venant equations, i.e.,  
 318 continuity and momentum equations for a shallow water wave. The 2-dimensional continuity  
 319 equation for a flood wave is:

$$320 \quad \frac{\partial h}{\partial t} + \frac{\partial q_x}{\partial x} + \frac{\partial q_y}{\partial y} = i_e \quad (5)$$

321 where  $h$  is the surface flow depth,  $q_x$  and  $q_y$  are the unit discharges in the x- and y-directions,  
 322 respectively, and  $i_e$  is the infiltration excess. Manning's equation which considers momentum loss  
 323 is used to calculate  $q$ . In the x-direction:

$$324 \quad q_x = \alpha_x h^\beta \quad (6)$$

325 Where  $\beta$  is a unit dependent coefficient equal to  $\frac{5}{3}$ , and

$$326 \quad \alpha_x = \frac{S_{fx}^{1/2}}{n_{ov}} \quad (7)$$

327 where  $n_{ov}$  is the tunable overland flow roughness coefficient. The momentum equation in the x-  
 328 direction is given by:

$$329 \quad S_{fx} = S_{ox} - \frac{\partial h}{\partial x} \quad (8)$$

330 where  $S_{fx}$  is the friction slope,  $S_{ox}$  is the terrain slope, and  $\frac{\partial h}{\partial x}$  is the change in surface flow depth  
 331 in the x-direction.

332 Off-the-shelf, WRF-Hydro does not output overland flow at terrain routing grids (100 m), however  
 333 it is computed in the background to determine channelized streamflow. One key advance made in  
 334 this work is that we modified WRF-Hydro source code to output overland flow. Overland flow  
 335 depth (m) was converted to overland discharge ( $\text{m}^3 \text{s}^{-1}$ ) by multiplying flow depth by grid cell area  
 336 ( $10,000 \text{ m}^2$ ) and dividing by the LSM time step (1 h).

337

### 338 **3.4 Channel routing**

339 If overland flow intersects grid cells identified as channel grids (2<sup>nd</sup> Strahler stream order and  
 340 above; pre-defined by the hydrologically conditioned USGS 30-m DEM), the channel routing  
 341 module routes the water as channelized streamflow using a 1-dimensional, explicit, variable time-  
 342 stepping diffusive wave formulation. Similarly, the continuity equation for channel routing is  
 343 given as:

344 
$$\frac{\partial A}{\partial t} + \frac{\partial Q}{\partial s} = q_l \quad (9)$$

345 and the momentum equation is given as:

346 
$$\frac{\partial Q}{\partial t} + \frac{\partial(\frac{\gamma Q^2}{A})}{\partial s} + gA \frac{\partial H}{\partial s} = -gAS_f \quad (10)$$

347 where  $s$  is the streamwise coordinate,  $H$  is water surface elevation,  $A$  is the flow cross-sectional  
 348 area calculated as  $(B_w + H z)H$  (Fig. B2),  $q_l$  is the lateral inflow rate into the channel grid,  $Q$  is  
 349 the flow rate,  $\gamma$  is a momentum correction factor,  $g$  is acceleration due to gravity, and  $S_f$  is the  
 350 friction slope computed as:

351 
$$S_f = \left(\frac{Q}{K}\right)^2 \quad (11)$$

352 where  $K$  is the conveyance computed from the Manning's equation:

353 
$$K = \frac{C_m}{n} AR^{2/3} \quad (12)$$

354 where  $n$  is the Manning's roughness coefficient,  $A$  is the channel cross-sectional area,  $R$  is the  
 355 hydraulic radius ( $A/P$ ),  $P$  is the wetted perimeter, and  $C_m$  is a dimensional constant (1.486 for  
 356 English units or 1.0 for SI units).

357

## 358 **4 Model simulation, calibration, and validation**

### 359 **4.1 Model domain**

360 The WRF-Hydro model domain spans regions in California including the Coast Ranges, Monterey  
 361 Bay, and the Central Valley, and covers several burn scars from the 2020 wildfire season (Fig. 1a).  
 362 Here we focus our analysis on the Dolan burn scar where the hazardous debris flows occurred (Fig.  
 363 1b).

364 To calibrate and validate WRF-Hydro output, we use soil moisture observations from two Physical  
 365 Sciences Laboratory (PSL) monitoring stations [i.e., Lockwood (lwd) and Gilroy (gry)] (Fig. 1a).  
 366 Due to the Mediterranean climate of California, many USGS stream gages experience low or no  
 367 flow during the dry season. In addition, many gages are under manual regulation to mitigate wet-  
 368 season flood risks and better distribute water resources. As such, it can be challenging to obtain  
 369 natural streamflow observations for model calibration. Here, three USGS stream gages [i.e.,  
 370 Arroyo Seco NR Greenfield, CA (ID 11151870), Arroyo Seco NR Soledad, CA (ID 11152000),  
 371 and Arroyo Seco BL Reliz C NR Soledad, CA (ID 11152050)] (Fig. 1a) on streams that have  
 372 measurable flows during our study period and are free of human regulation are used. These gages  
 373 are located downstream of the Dolan burn scar and hence are useful in calibrating the parameters  
 374 associated with burn scar effects. The PSL soil moisture observations were recorded at 2-minute

375 intervals and USGS streamflow gage data were recorded at 15-minute intervals, but we perform  
376 all observation-model comparisons at hourly-mean resolution.

377

378

#### 379 **4.2 Baseline simulation and soil moisture calibration**

380 WRF-Hydro was initialized with National Centers for Environmental Prediction (NCEP) FNL  
381 (Final) Operational Global Analysis data and was run from January 1–31, 2021. We performed the  
382 baseline simulation by modifying WRF-Hydro default parameters (Table B3) based on a  
383 calibration using soil moisture observations from stations lwd and gry. Neither PSL station is  
384 located in a burn scar. Since the baseline simulation includes no postfire characteristics, it can also  
385 be regarded as the “pre-fire” scenario. Soil moisture at 10 cm below ground in the baseline  
386 simulation was calibrated by performing a domain-wide adjustment of soil porosity and grain size  
387 distribution index at the simulation start (Table B3). We then allowed the model to spin up from  
388 January 1–10 before using January 11–31 for validation. Using a relatively short spin-up period is  
389 justified because prior to the AR event, little rain fell on the Dolan burn scar (i.e., ~400 mm of  
390 rainfall fell from June to December 2020). As such, in the months preceding the debris flow events,  
391 soil moisture observations indicate already dry conditions prior to our 10 day spin up.

392

393 After calibration, the simulated soil moisture closely mimics ground-based PSL observations (Fig.  
394 4). Both the observed magnitude and variability are well captured, with the simulated  $\pm 1$  standard  
395 deviation envelope largely encompassing PSL observations during the AR. Model performance  
396 was evaluated using four quantitative metrics, i.e., correlation coefficient ( $r$ ), root mean square  
397 error (RMSE), mean absolute error (MAE), and Kling-Gupta efficiency (KGE; Gupta et al., 2009;  
398 Kling et al., 2012). KGE has previously been used in soil moisture calibration applications (e.g.,  
399 Lahmers et al., 2019; Vergopolan et al., 2020) and is computed as follows:

400

$$401 \quad KGE = 1 - \sqrt{(r - 1)^2 + (\alpha - 1)^2 + (\beta - 1)^2} \quad (13)$$

402

403 where  $r$  is the correlation coefficient between the observation and simulation,  $\alpha$  is the ratio of the  
404 standard deviation of simulation to the standard deviation of observation, and  $\beta$  is the ratio of the  
405 mean of simulation to the mean of observation. KGEs close to 1 indicate a high-level consistency  
406 between the simulation and observation, while negative KGEs indicate poor model performance  
407 (Andersson et al., 2017; Schönfelder et al., 2017).

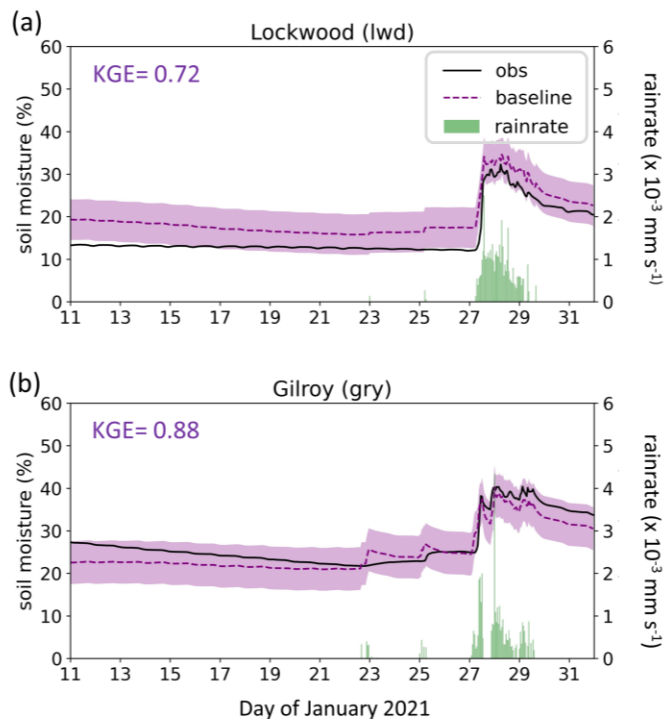
408

409 The model’s ability to simulate soil moisture substantially improves after calibration (Fig. 4; Table  
410 1). KGE values approach 1 (0.72 at lwd and 0.88 at gry), indicating that WRF-Hydro adequately  
411 simulates the hydrologic environment and its response to meteorological changes.

412

413  
414

MRMS precipitation, observed and simulated soil moisture



415 **Fig. 4|** Precipitation, observed and simulated soil moisture at two PSL soil moisture stations.  
 416 January 11–31, 2021 MRMS precipitation (green bars) and observed (black line) and simulated  
 417 volumetric soil moisture 10 cm below ground in the baseline simulation (purple dashed line) at  
 418 PSL sites (a) Lockwood (lwd) and (b) Gilroy (gry). Envelope of purple shading depicts  $\pm 1$  standard  
 419 deviation of model simulated soil moisture. KGE scores are provided at top left for each station.  
 420

421  
422  
423  
424  
425  
426

*Table 1*  
*Evaluation metrics of simulated soil moisture and streamflow*

Soil moisture (Default / Baseline)				
Station	<i>r</i>	RMSE	MAE	KGE
lwd	0.97 / <u>0.98</u>	7.06 / <u>4.32</u>	5.21 / <u>4.16</u>	0.10 / <u>0.72</u>

<b>gry</b>	0.94 / 0.94	5.19 / <u>2.53</u>	11.12 / <u>2.31</u>	0.80 / <u>0.88</u>
<b>Streamflow (Baseline / Burn scar)</b>				
<b>Station</b>	<b><i>r</i></b>	<b>RMSE</b>	<b>MAE</b>	<b>NSE</b>
<b>1870</b>	0.28 / <u>0.93</u>	39.29 / <u>14.69</u>	16.05 / <u>6.14</u>	-0.17 / <u>0.84</u>
<b>2000</b>	0.26 / <u>0.86</u>	51.22 / <u>24.92</u>	20.11 / <u>10.00</u>	-0.15 / <u>0.73</u>
<b>2050</b>	0.25 / <u>0.81</u>	49.96 / <u>27.43</u>	19.64 / <u>11.65</u>	-0.38 / <u>0.53</u>

427  
428 **Table 1|** Quantitative evaluation metrics for the simulated soil moisture and streamflow when  
429 compared against observations. The metrics include the Pearson correlation coefficient (*r*), root  
430 mean square error (RMSE), and mean absolute error (MAE). In addition, the comprehensive  
431 metrics Kling-Gupta efficiency (KGE) and Nash-Sutcliffe efficiency (NSE) are used to evaluate  
432 model-simulated soil moisture and streamflow, respectively. For soil moisture, the numbers in  
433 front of “/” are calculated between the default run (i.e., uncalibrated run) and the observations,  
434 whereas the numbers following “/” are the corresponding values in the baseline simulation (the  
435 purple dashed line in Fig. 4). For streamflow, the numbers in front of “/” are computed between  
436 the baseline run (purple dashed line in Fig. 6) and the observations, while the numbers behind “/”  
437 are for burn scar simulation (red line in Fig. 6). If the model performance regarding a certain metric  
438 is enhanced in the burn scar simulation, the number after “/” is underlined.  
439

#### 440 **4.3 Burn scar simulation and streamflow calibration**

441 To simulate effects of wildfire burn scars on hydrologic processes and debris flow susceptibility,  
442 we made two modifications to the baseline simulation soil moisture calibrated model configuration.  
443 First, we changed the land cover type within the burn scar perimeter to its nearest LSM analogue,  
444 i.e., “barren and sparsely vegetated”. The switch to barren land causes: (1) height of the canopy  
445 (HVT) to decrease to 0.5 m; (2) maximum rate of carboxylation at 25°C (VCMX25) to decrease  
446 to 0  $\mu\text{mol CO}_2/(\text{m}^2 \cdot \text{s})$ ; and (3) overland flow roughness coefficient (OV\_ROUGH2D) to decrease  
447 to 0.035 (Fig. 5a–c) from default values (Fig. B4 and Table B2).  
448

449 The second adjustment was to decrease soil infiltration rates within the burn scar perimeter,  
450 achieved by reducing soil saturated hydraulic conductivity (DKSAT; Fig. 5d; Scott & van Wyk,  
451 1990; Cerdà, 1998; Robichaud, 2000; Martin & Moody, 2001) from default values (Table B3).  
452 Consistent with the hydrophobicity of burned soils, we calibrate the burn scar simulation by  
453 systematically exploring a range of burn scar area saturated hydraulic conductivities (0 to  $3 \times 10^{-7}$   
454  $\text{m s}^{-1}$  with a  $5 \times 10^{-8}$   $\text{m s}^{-1}$  increment), with the goal of reproducing streamflow behavior similar to  
455 USGS gage observations. We found that a value of  $1.5 \times 10^{-7}$   $\text{m s}^{-1}$  gives the highest Nash-Sutcliffe  
456 efficiency (NSE; Nash & Sutcliffe, 1970) across all three USGS stream gages (Table 1). NSE and  
457 KGE are the two most widely used metrics for calibration and evaluation of hydrologic models.



458 The NSE has previously been used in streamflow calibration applications (e.g., Xia et al., 2012;  
459 Bitew & Gebremichael, 2011), and it is calculated as follows:

460

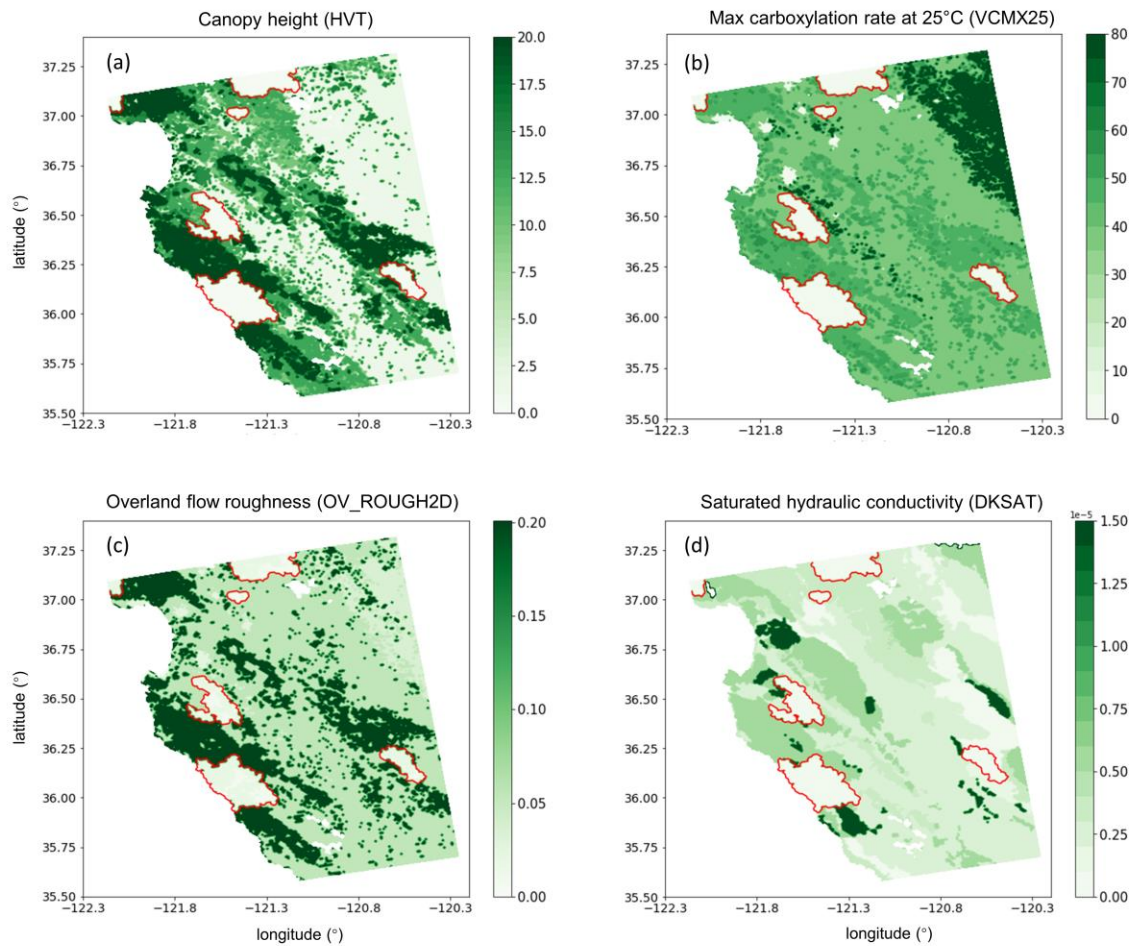
$$461 \quad NSE = 1 - \frac{\sum_{t=1}^{t=T} (Q_{sim}(t) - Q_{obs}(t))^2}{\sum_{t=1}^{t=T} (Q_{obs}(t) - \overline{Q_{obs}})^2} \quad (14)$$

462

463 where  $T$  is the length of the time series,  $Q_{sim}(t)$  and  $Q_{obs}(t)$  are the simulated and observed  
464 discharge at time  $t$ , respectively, and  $\overline{Q_{obs}}$  is the mean observed discharge. By definition, NSEs of  
465 1 indicate perfect correspondence between the simulated and observed streamflow. Positive NSEs  
466 indicate that the model streamflow has a greater explanatory power than the mean of the  
467 observations, whereas negative NSEs represent poor model performance (Moriasi et al., 2007;  
468 Schafli & Gupta, 2007). When burn scar characteristics are included, evaluation metrics including  
469  $r$ , RMSE, and MAE all improve, while NSEs increase from negative values in the baseline to 0.84,  
470 0.73, and 0.53 at gages 1870, 2000, and 2050, respectively. Higher correlation and NSE scores  
471 and lower errors indicate the above mentioned burn scar parameter changes improve the model's  
472 ability to simulate streamflow observations downstream of the burn scar (Table 1).

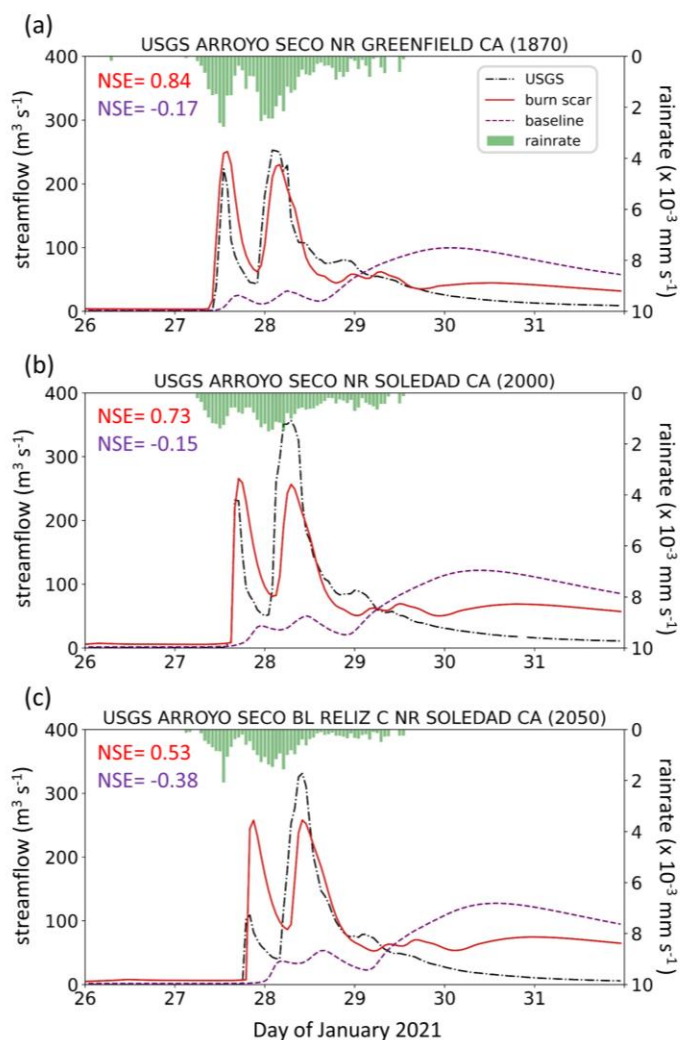
473

### Parameter changes accounting for burn scar characteristics



474  
475 **Fig. 5|** Parameter setting in the WRF-Hydro burn scar simulation. (a) The height of the canopy  
476 (HVT; m; shading), (b) maximum rate of carboxylation at 25°C (VCMX25;  $\mu\text{mol CO}_2/(\text{m}^2 \cdot \text{s})$ ;  
477 shading), (c) overland flow roughness coefficient (OV\_ROUGH2D; shading), and (d) saturated  
478 hydraulic conductivity (DKSAT;  $\text{m s}^{-1}$ ; shading) in the burn scar simulation.

### MRMS precipitation, observed and simulated streamflow



479  
 480 **Fig. 6** Precipitation, observed and simulated streamflow at three USGS stream gages. January 26–  
 481 31, 2021 MRMS precipitation (green bars), observed (black dash dotted line) and simulated  
 482 streamflow in baseline simulation (purple dashed line) and burn scar simulation (red line) at (a)  
 483 Arroyo Seco NR Greenfield, CA (ID 11151870), (b) Arroyo Seco NR Soledad, CA (ID 11152000),  
 484 and (c) Arroyo Seco BL Reliz C NR Soledad, CA (ID 11152050). NSE scores for baseline (purple)  
 485 and burn scar simulations (red) are shown at top left.  
 486

## 487 **5 Results**

### 488 **5.1 Hydrologic response due to burn scar incorporation**

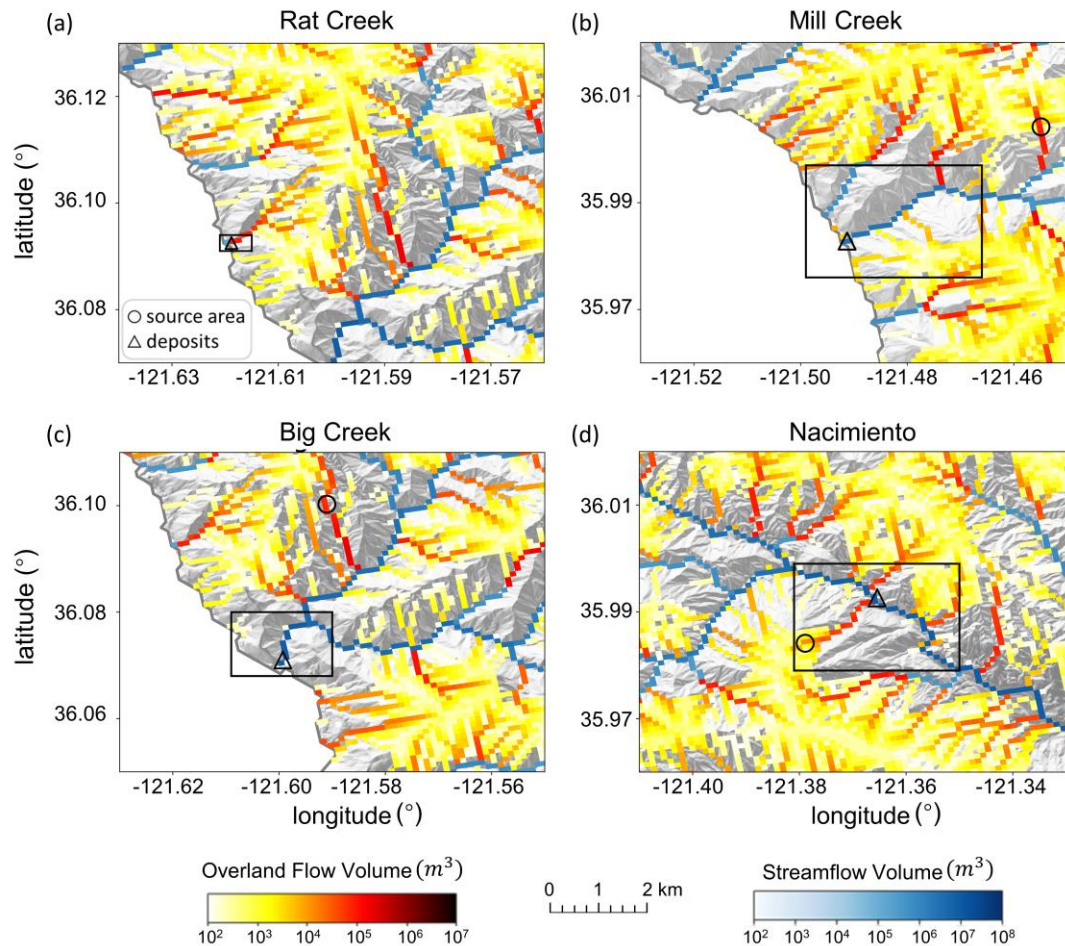
489 The pre-fire baseline simulation fails to capture the hydrologic behavior observed at the USGS  
490 gages located within the burn scar (Fig. 6). Incorporation of burn scar characteristics substantially  
491 alters the hydrologic response of the model and provides much higher fidelity streamflow  
492 simulations (Fig. 6). Observed hydrographs are characterized by two early streamflow peaks  
493 related to two precipitation bursts on January 27<sup>th</sup> and 28<sup>th</sup>. Our burn scar simulation captures this  
494 behavior, while the baseline simulation streamflow peaks just once, with a lower magnitude and  
495 an ~3-day lag after peak precipitation (Fig. 6). The steep rising limbs and high magnitude discharge  
496 peaks of the burn scar hydrograph are indicative of flash flooding. Compared with the pre-fire  
497 baseline scenario, the burn scar's barren land and low infiltration rate substantially accelerate  
498 drainage rates and increase discharge volume into stream channels.

499

### 500 **5.2 Hydrologic response at four debris flow sites**

501 Mill Creek, Big Creek, and Nacimiento deposits are located in channels of 2<sup>nd</sup> Strahler stream  
502 order or above so they are simulated as channelized streamflow in our WRF-Hydro simulations.  
503 Due to its low stream order (1<sup>st</sup> Strahler stream order), Rat Creek is modeled entirely as overland  
504 flow in our WRF-Hydro simulations. At the four debris flow sites, we use three metrics to  
505 characterize hydrologic anomalies: (1) accumulated runoff volume, (2) peak discharge, and (3)  
506 time to peak discharge. Fig. 7 depicts accumulated channelized discharge volume (blue shading)  
507 and accumulated overland discharge volume (yellow-red shading) from January 27<sup>th</sup> 00:00 to 28<sup>th</sup>  
508 12:00 near the four debris flow sites in the burn scar simulation. Accumulation time period is  
509 chosen such that it covers the first two runoff surges in the simulated hydrographs which are likely  
510 associated with debris flows (Fig. 8) given that nearly concurrent peak rainfall intensity and peak  
511 discharge is a signature characteristic of debris flows (Kean et al., 2011). Runoff volume is on the  
512 order of  $10^4 \text{ m}^3$  at Rat Creek and  $10^6 \text{ m}^3$  at the other three sites.

### Simulated overland flow and streamflow in burn scar simulation

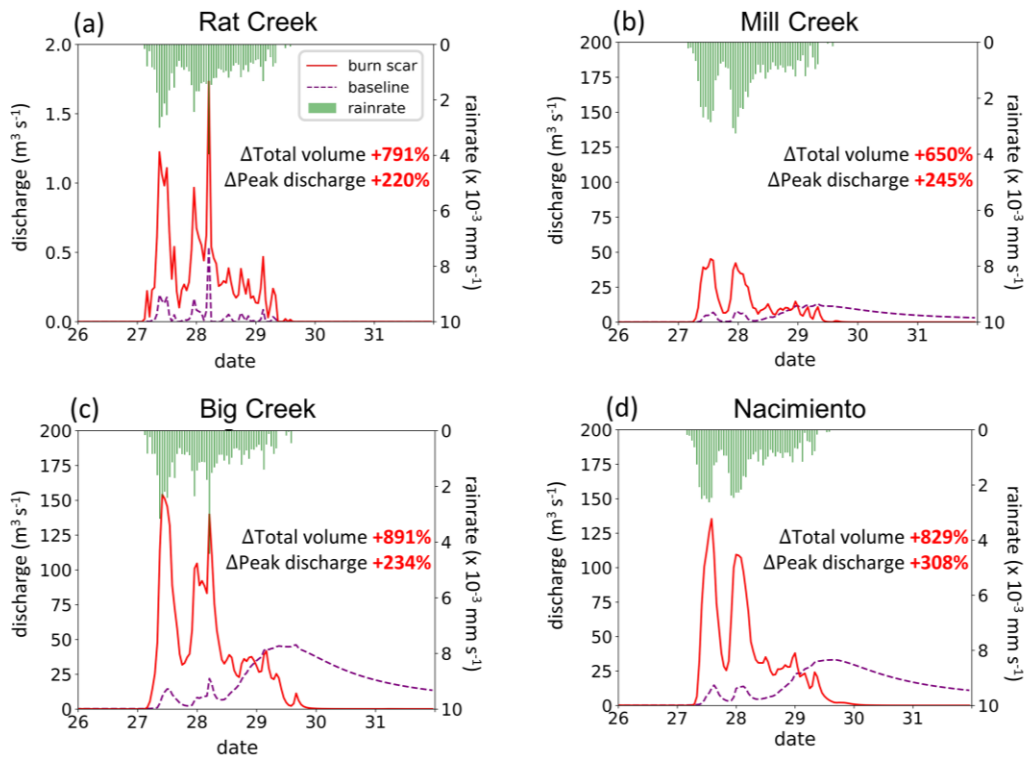


513  
 514 **Fig. 7** | WRF-Hydro simulated overland flow and streamflow in the burn scar simulation. (a)–(d)  
 515 Total volume of accumulated overland flow (yellow-red shading) and streamflow (blue shading)  
 516 between January 27<sup>th</sup> 00:00 and 28<sup>th</sup> 12:00 at four debris flow sites draped over a hillshade of  
 517 topography. Black rectangles correspond to domains in Fig. 3a–d. Black circles and triangles  
 518 indicate debris flow source areas and deposits, respectively.

519  
 520  
 521 Dramatic hydrographic changes after inclusion of burn scar characteristics are simulated at debris  
 522 flow source areas (Fig. B6 and Table B4) and deposition sites (Fig. 8 and Table 2). WRF-Hydro  
 523 facilitates investigation of the hydrologic response at triggering and deposit locations and along  
 524 the runout path. Here, to emphasize the high susceptibility downstream, our analysis is focused on  
 525 debris flow deposits. At Rat Creek, where a section of CA1 collapsed, the magnitude of discharge  
 526 substantially increases, and overland flow surges are concurrent with rainfall bursts (Fig. 8a). Total

527 discharge accumulated during the AR event increases approximately eight-fold (791%), and peak  
 528 discharge more than triples compared to the baseline simulation (Fig. 8a and Table 2). At Mill  
 529 Creek, Big Creek, and Nacimiento, baseline hydrographs are characterized by less variability,  
 530 muted responses to two early precipitation bursts, and a delayed third discharge peak that does not  
 531 occur until ~3 days after AR passage (Fig. 8b–d). Maximum discharge peaks in the baseline  
 532 hydrographs lag those in the burn scar simulation by ~2 days (Fig. 8b–d; Table 2). In the burn scar  
 533 simulation, total volume substantially increases at the three channelized sites – total volume  
 534 increases ~650% at Mill Creek, ~891% at Big Creek, and ~829% at Nacimiento (Fig. 8b–d and  
 535 Table 2), and the absolute increase in volume is on the order of  $10^6 \text{ m}^3$  (Table 2). Peak discharge  
 536 more than triples at Mill Creek and Big Creek and more than quadruples at Nacimiento.  
 537 Additionally, response times of the peak in discharge to the peak in precipitation decrease to less  
 538 than an hour, highlighting the simulated flashiness of the burned catchments.  
 539  
 540  
 541

MRMS precipitation and simulated discharge



542  
 543  
 544 **Fig. 8** | WRF-Hydro simulated discharge time-series at four debris flow deposition locations. (a)–  
 545 (d) MRMS precipitation (green bars) and simulated discharge time-series for January 26<sup>th</sup> 00:00



546 to 31<sup>st</sup> 23:00 at (a) Rat Creek, (b) Mill Creek, (c) Big Creek, and (d) Nacimiento deposition  
 547 locations (black triangles in Fig. 7a–d) in baseline simulation (purple dashed line) and burn scar  
 548 simulation (red line).

549  
 550

551 *Table 2*

552 *The total runoff volume, peak discharge, and peak timing at debris-flow deposits*

Site name	Baseline simulation			Burn scar simulation			
	Total volume (m <sup>3</sup> )	Peak discharge (m <sup>3</sup> s <sup>-1</sup> )	Highest peak timing	Total volume (m <sup>3</sup> )	Peak discharge (m <sup>3</sup> s <sup>-1</sup> )	1 <sup>st</sup> Peak timing	2 <sup>nd</sup> Peak timing
<b>Rat Creek</b>	6,897	0.54	28 <sup>th</sup> 05:00	61,425 (+791%)	1.73 (+220%)	27 <sup>th</sup> 09:00	28 <sup>th</sup> 05:00
<b>Mill Creek</b>	312,925	13.10	29 <sup>th</sup> 08:00	2,347,457 (+650%)	45.21 (+245%)	27 <sup>th</sup> 13:00	27 <sup>th</sup> 23:00
<b>Big Creek</b>	842,808	46.10	29 <sup>th</sup> 16:00	8,354,095 (+891%)	154.10 (+234%)	27 <sup>th</sup> 10:00	28 <sup>th</sup> 05:00
<b>Nacimiento</b>	743,531	33.15	29 <sup>th</sup> 16:00	6,904,706 (+829%)	135.41 (+308%)	27 <sup>th</sup> 14:00	28 <sup>th</sup> 00:00

553

554 **Table 2**| The total runoff volume, peak discharge, and peak timing in the baseline and burn scar  
 555 simulations from January 27<sup>th</sup> 00:00 to 31<sup>st</sup> 23:00 at deposition sites of Rat Creek, Mill Creek, Big  
 556 Creek, and Nacimiento debris flows (black triangles in Fig. 7a–d). The peak timing shown in the  
 557 baseline simulation is for the highest peak. The percent change of the total volume and peak  
 558 discharge in the burn scar simulation relative to the baseline simulation are shown in parentheses.

559  
 560

561 **5.3 Debris flow susceptibility assessment for the Dolan burn scar**

562 Since high magnitude runoff is often the cause and precursor of runoff-generated debris flows in  
 563 burned areas (Cannon et al., 2003, 2008; Rengers et al., 2016), we use simulated accumulated  
 564 volume of overland flow and streamflow to assess runoff-generated debris flow susceptibility  
 565 under pre-fire (i.e., baseline; Fig. 9a&d) and postfire (i.e., burn scar simulation; Fig. 9b&e)  
 566 conditions. We assess changes at both stream and catchment levels and use the difference between  
 567 burn scar and baseline simulations to assess added debris flow susceptibility (Fig. 9c&f).  
 568 Consistent with the increasing erosive and entrainment power associated with increasing discharge,  
 569 our debris flow susceptibility increases as the accumulated discharge volume increases. To reduce  
 570 the effects of catchment size on the volume-based susceptibility levels, we normalize a

571 catchment's discharge volume by the area of the catchment (Santi & Morandi, 2013; Fig. 9d–f).  
572 Non-normalized catchment susceptibility maps are also provided (Fig. B7).

573  
574 In the pre-fire baseline simulation, the AR-induced precipitation produces lower debris flow  
575 susceptibility over most of the domain, but elevated susceptibility along stream channels (Fig. 9a).  
576 We note no substantial differences between areas in or out of the burn scar. In the burn scar  
577 simulation, debris flow susceptibility levels increase across the Dolan burn scar and along channels  
578 outside but downstream of the burn scar (Fig. 9b–c). The discharge volume increases by an order  
579 of magnitude near Rat Creek, Big Creek, Mill Creek, and Nacimiento. Within the burn scar,  
580 susceptibility along major stream channels, such as the Nacimiento River and San Antonio River  
581 increase. Outside the burn scar, susceptibility levels along river channels downstream of the burn  
582 scar, such as the Arroyo Seco River, also increase (Fig. 9c).

583  
584 At the catchment level, debris flow susceptibility is assessed using accumulated discharge volumes  
585 normalized by catchment areas (Fig. 9d–f). Accumulated discharge volumes are calculated at the  
586 outlet of each catchment between January 27<sup>th</sup> 00:00 to 28<sup>th</sup> 12:00. The catchment-area normalized  
587 volume is then used as the susceptibility index and is classified into five categories based on equal  
588 intervals on log<sub>10</sub> scale. The susceptibility categorization follows: “very low” ( $\sim 10^3 \text{ m}^3 \text{ km}^{-2}$ ), “low”  
589 ( $\sim 10^4 \text{ m}^3 \text{ km}^{-2}$ ), “medium” ( $\sim 10^5 \text{ m}^3 \text{ km}^{-2}$ ), “high” ( $\sim 10^6 \text{ m}^3 \text{ km}^{-2}$ ), and “very high” ( $\sim 10^7 \text{ m}^3 \text{ km}^{-2}$ ).  
590 In the baseline simulation, majority of catchments are subject to low or very low debris flow  
591 susceptibility with total normalized discharge volume less than  $10^4 \text{ m}^3 \text{ km}^{-2}$  (Fig. 9d). In the burn  
592 scar simulation, about half of the catchments within the Dolan burn scar have medium  
593 susceptibility or above, and about 1/4 of basins are subject to high debris flow susceptibility (Fig.  
594 9e). The additional debris flow susceptibility brought about by the inclusion of wildfire burn scar  
595 characteristics is substantial (Fig. 9f).

596 To summarize changes in debris flow susceptibility as a result of including burn scar  
597 characteristics in WRF-Hydro simulations, we create distributions of pre-fire baseline and burn  
598 scar catchment-area normalized discharge from the 404 catchments located within the Dolan burn  
599 scar perimeter (Fig. 10). After incorporating burn scar characteristics, the full distribution shifts to  
600 the right, indicating increased susceptibility levels – a shift considered robust by a Student's t-test  
601 ( $p$  value:  $4.6\text{E-}45$ ). A quantitative assessment of this shift indicates that the mean catchment area  
602 normalized discharge volume increases by  $\sim 1300\%$  while the standard deviation increases  
603  $\sim 1400\%$  (Table 3). We also assess shifts at a range of distribution percentiles: 5P: 148%, 25P:  
604 725%, 50P: 924%, 75P: 980%, and 95P: 1300% (Table 3). In the burn scar simulation, nearly half  
605 of catchments have normalized volumes  $> 10^5 \text{ m}^3 \text{ km}^{-2}$  (i.e., medium susceptibility) and about 1/4  
606 of catchments have volumes  $> 10^6 \text{ m}^3 \text{ km}^{-2}$  (i.e., high susceptibility) – values that correspond to  
607 the 75P and 90P of the baseline simulation, respectively. Disproportionate shifting of the right tail  
608 of the distribution suggests that extreme debris flow susceptibility increases non-linearly under  
609 simulated burn scar conditions.



610 *Table 3*

611 *Statistics of catchment area-normalized discharge volume in baseline and burn scar simulations*

	<b>mean</b>	<b>std</b>	<b>5P</b>	<b>25P</b>	<b>50P</b>	<b>75P</b>	<b>95P</b>
<b>Baseline simulation</b> (m <sup>3</sup> km <sup>-2</sup> )	380k	± 1.6M	0.6k	3.7k	13k	120k	2.1M
<b>Burn scar simulation</b> (m <sup>3</sup> km <sup>-2</sup> )	5.5M	± 23.0M	1.5k	30.7k	135k	1.3M	29.1M
<b>Relative percent change</b>	1300%	1400%	148%	725%	924%	980%	1300%

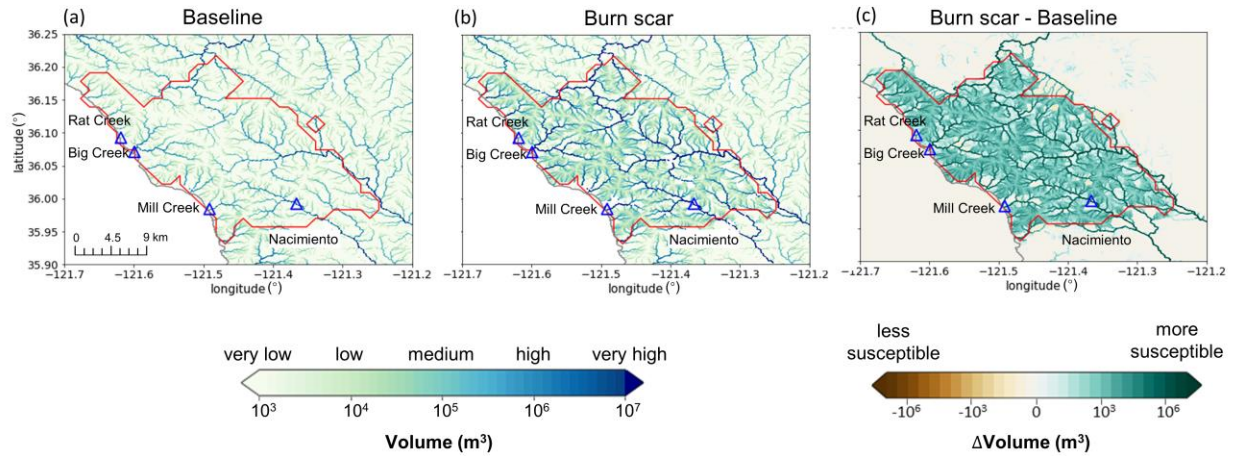
612 **Table 3**| Statistics, including the mean, standard deviation (std), 5P, 25P, 50P, 75P, and 95P, of  
613 the catchment-area normalized discharge volume for all basins within the Dolan burn scar in the  
614 baseline and burn scar simulation and their relative percent changes.

615

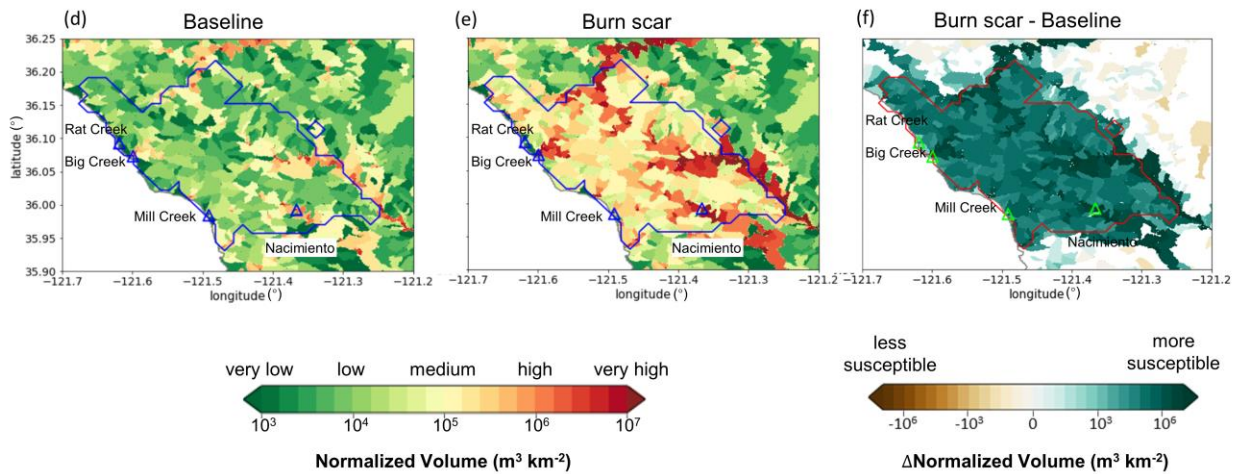
616 Our catchment-area normalized discharge volume-based susceptibility assessment also indicates  
617 that the catchments containing Mill Creek, Big Creek, and Nacimiento have high or very high  
618 susceptibility (Fig. 9d–f), consistent with our (limited) debris flow observations. Other areas with  
619 elevated susceptibility include catchments containing the Arroyo Seco and San Antonio Rivers.  
620 Beyond the burn scar perimeter, effects of fire expand to adjacent and downstream catchments,  
621 and some drainage basins along the Arroyo Seco and Nacimiento Rivers are simulated to have  
622 very high susceptibility, i.e., normalized discharge volumes in excess of 10<sup>7</sup> m<sup>3</sup> km<sup>-2</sup> (Fig. 9e&f).

623

## Postfire Debris Flow Susceptibility

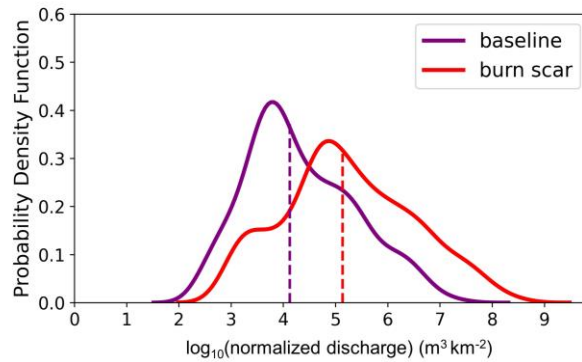


## Catchment-area Normalized Postfire Debris Flow Susceptibility



624  
625

626 **Fig. 9|** Discharge volume-based postfire debris flow susceptibility. Debris flow susceptibility at  
627 individual stream level for the (a) baseline, (b) burn scar, and (c) difference between burn scar and  
628 baseline simulations. Susceptibility is estimated as total discharge volume from January 27th 00:00  
629 to 28th 12:00. (d)–(f) Normalized debris flow susceptibility by catchment area at catchment level.  
630 For each catchment, the susceptibility is determined by total discharge volume at the catchment  
631 outlet from January 27th 00:00 to 28th 12:00 divided by catchment area.



632

633 **Fig. 10** | Distributions of accumulated discharge volumes at the outlet of the 404 catchments  
 634 normalized by upstream catchment areas within Dolan burn scar in the baseline simulation (purple  
 635 line) and in the burn scar simulation (red line). Dashed vertical lines indicate median values.

636

## 637 **6 Discussion**

638 Given the historic and growing frequency of wildfires in the western U.S. (Williams et al., 2019;  
 639 Goss et al., 2020; Swain 2021) and globally (Flannigan et al., 2013; Jolly et al., 2015), developing  
 640 tools to investigate, better understand, and potentially predict changes in burn scar hydrology and  
 641 natural hazards at regional scales is critical. Here, we demonstrate the first use of WRF-Hydro to  
 642 simulate the susceptibility of a burn scar to postfire debris flows during a landfalling AR. We  
 643 augmented the default version of WRF-Hydro to output overland flow and to replicate burn scar  
 644 behavior by adjusting vegetation type and infiltration rate parameters. WRF-Hydro simulations  
 645 were validated against PSL soil moisture and USGS streamflow observations before we used  
 646 simulated streamflow and overland flow volumes to characterize debris flow susceptibility. A  
 647 comparison between baseline and burn scar simulations demonstrated that changes in hydraulic  
 648 properties of burned areas causes drastic changes in surface flows, including faster discharge  
 649 response times, and greater peak discharge and total volumes, consistent with findings from  
 650 previous postfire hydrology studies (Anderson et al., 1976; Scott, 1993; Meixner & Wohlgenuth,  
 651 2003; Kean et al., 2011; Kinoshita & Hogue, 2015; Brunkal & Santi, 2016; Williams et al., 2022).  
 652 At the catchment level, for the 404 catchments located within the Dolan burn scar, median  
 653 catchment area-normalized volume increases nine-fold relative to the baseline. In addition, Mill  
 654 Creek, Big Creek, and Nacimiento basins were simulated to have high-to-very high debris flow  
 655 susceptibility, corresponding well with identified debris flow occurrences.

656

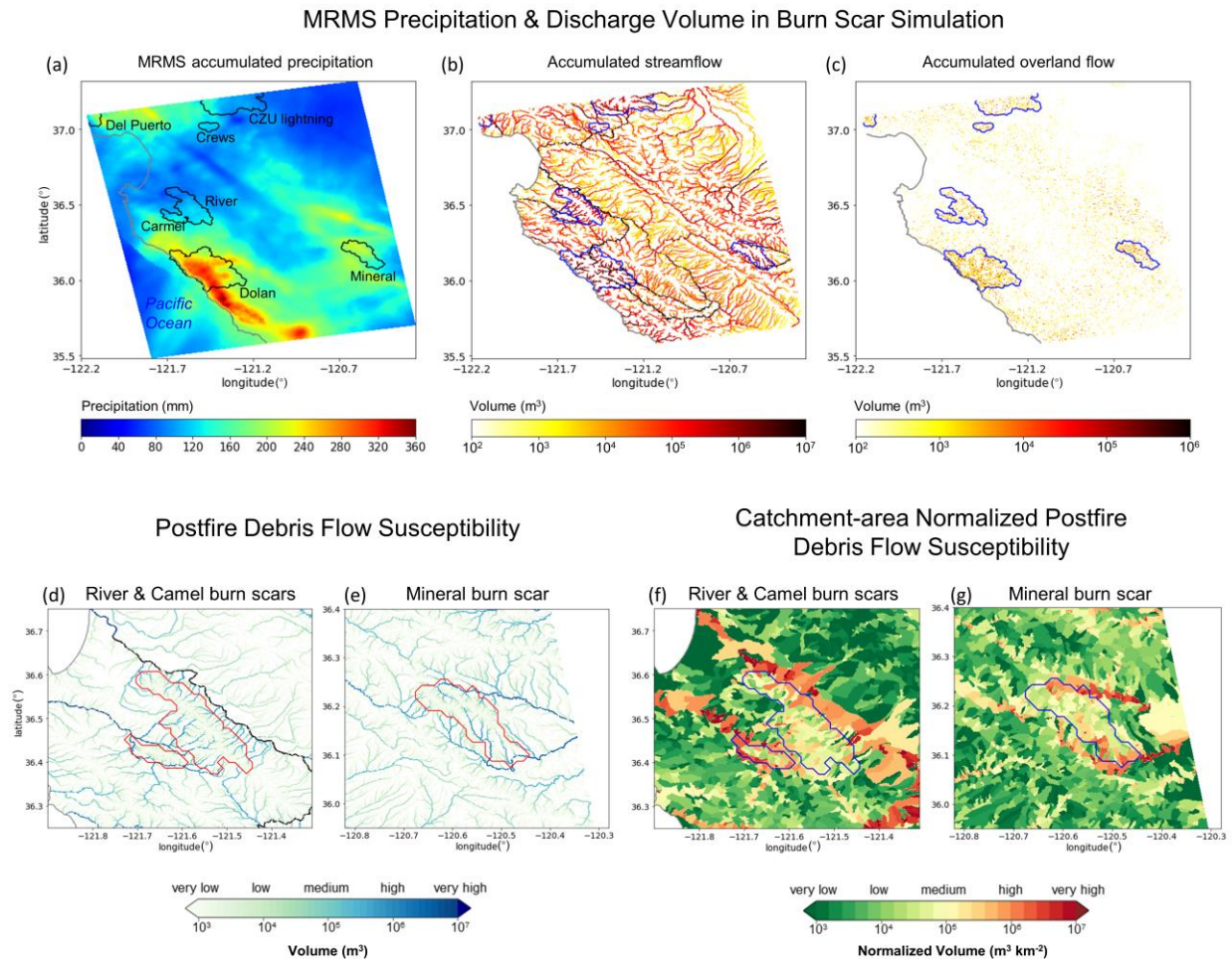
657 Despite methodological differences, our debris flow susceptibility map for this AR event is  
 658 generally consistent with the USGS' postfire, pre-AR, design-storm-based preliminary hazard  
 659 assessment (USGS, 2020). As described above, USGS preliminary hazard assessments use logistic

660 regression models to estimate the likelihood of debris flow occurrence and multivariate linear  
661 regression models to estimate debris flow volumes. The USGS empirical approach is trained on  
662 historical western U.S. debris flow occurrence and magnitude data and incorporates burn scar soil  
663 erodibility and burn severity data (Cannon et al., 2010; Gartner et al., 2014; Staley et al., 2016).  
664 For precipitation, the USGS assessment utilizes a design storm approach that assumes 1–5 year  
665 return interval magnitude precipitation falls uniformly over a region/burn scar (USGS, 2020). For  
666 the Dolan burn scar, both assessments find that large stream channels had relatively higher  
667 susceptibility than small streams or overland areas. However, a close comparison of the two maps  
668 reveals differences in spatial distribution of hazardous catchments. In the USGS assessment,  
669 higher likelihood is predicted north and southeast of the burn scar, whereas in our assessment the  
670 highest susceptibility occurs along major stream channels. We hypothesize that USGS-assessed  
671 areas of higher hazard potential are related to their use of spatially uniform design-storm  
672 precipitation (see Fig. 2 for MRMS precipitation footprint) and burn severity data (Burned Area  
673 Emergency Response, 2020).

674  
675 Comparison with the USGS hazard assessment framework suggests room for improvement in  
676 WRF-Hydro-based assessments (i.e., inclusion of burn severity and soil erodibility data), but also  
677 highlights the potential utility of working with spatially-distributed and time-varying precipitation.  
678 However, this also means the accuracy of WRF-Hydro predictions depends on the accuracy of  
679 precipitation forcing, and in our hindcast application, MRMS precipitation data (Appendix A).  
680 Accordingly, our WRF-Hydro-based assessment could benefit from precipitation products  
681 mosaiced from various sources to constrain precipitation-based uncertainties (e.g., gauge-  
682 corrected and/or Mountain Mapper MRMS), although the long processing time of these datasets  
683 inhibits timely post-event assessments.

684 In addition to the above results focused primarily on the Dolan burn scar, a key feature of WRF-  
685 Hydro is its ability to simulate the land surface hydrology of expansive geographic domains, e.g.,  
686 NOAA runs the National Water Model over the entire continental U.S. Development of tools  
687 capable of regional susceptibility assessments is crucial, particularly in a wildfire-prone region  
688 like California, due to the large spatial scale, diverse morphology, and often tight spatial gradients  
689 of precipitation events and their interactions with geographically widespread wildfire burn scars.  
690 For example, landfalling ARs are often long (1000s of km) filament-like systems with  
691 heterogeneous intensity gradients along their length. As a demonstration of wide geographic  
692 applicability, we assess susceptibility over our full model domain which includes more than 10,000  
693 catchments and a number of 2020 wildfire burn scars in addition to the Dolan burn scar (Fig 11).  
694 The domain-wide analysis reveals elevated discharge volume, i.e., elevated susceptibility, in areas  
695 of high precipitation and in burned terrains (Figs. 11a–c). We highlight channelized and  
696 catchment-area normalized debris flow susceptibility in non-Dolan burn scar sites in Figs. 11d–g.  
697 In an operational forecast context, the ability to simulate landslide and debris flow susceptibilities  
698 and hazards over numerous catchments at meteorologically appropriate scales represents a step-  
699 change in the field. We argue that our demonstration of WRF-Hydro’s debris flow susceptibility

700 hindcast capabilities should motivate further exploration and development for potential use in  
 701 operational hazard forecasting.



702

703 **Fig. 11** MRMS accumulated precipitation and discharge volume informed regional debris flow  
 704 susceptibility. (a) MRMS accumulated precipitation during January 27<sup>th</sup> 00:00 to 29<sup>th</sup> 23:00 over  
 705 the model domain (shading; mm). Names of burn scars are labeled in black. (b) Accumulated  
 706 streamflow (yellow-to-red shading;  $m^3$ ) and (c) accumulated overland flow from 27<sup>th</sup> 00:00 to 28<sup>th</sup>  
 707 12:00 over the model domain (yellow-to-red shading;  $m^3$ ). (d)–(e) Stream-level postfire debris  
 708 flow susceptibility as Fig. 9b but for River and Camel burn scars. (f)–(g) Catchment-area  
 709 normalized debris flow susceptibility as Fig. 9e but for River and Camel burn scars. Wildfire  
 710 perimeters of 2020 wildfire season are outlined in black in (a), in blue in (b), (c), (f), and (g), and  
 711 in red in (d) and (e). The coastline of California is depicted in grey.

712

713 In addition to investigating the operationalization of WRF-Hydro’s natural hazard prediction  
 714 capabilities, we note that our susceptibility-focused methodology could be advanced to hazard



715 assessment, in line with current USGS products. The USGS Emergency Assessment of Postfire  
716 Debris-flow Hazard predicts debris flow volume and likelihood. To advance from susceptibility to  
717 hazard assessment, our methodology would need to incorporate both debris flow volume estimates  
718 and occurrence likelihoods. In the following, we highlight research directions that could help  
719 advance our susceptibility-focused methodological framework. WRF-Hydro is a water-only model.  
720 While water-only models have been widely used to investigate and better understand debris flow  
721 dynamics (Arattano & Savage, 1994; Tognacca et al., 2000; Arattano & Franzi, 2010; Rengers et  
722 al., 2016; McGuire & Youberg, 2020; Di Cristo et al., 2021), sediment supply, soil erodibility, and  
723 other sedimentological factors play important roles in determining the potential for and severity of  
724 mass failure events (McGuire et al., 2017). Developing a runoff-generated debris flow model that  
725 couples hydrologic and sediment erosion and transport processes could help to characterize  
726 postfire debris flow volumes. Indeed, previous efforts have demonstrated the capacity to couple  
727 WRF-Hydro with sediment flux models (Yin et al., 2020; Shen et al., 2021). In addition to  
728 sediments, burn scar ash can comprise a substantial fraction of the total debris flow volume (e.g.,  
729 Reneau et al., 2007). As such, efforts to constrain ash availability and entrainment in hydrologic  
730 flows could prove fortuitous in hazard assessment and prediction efforts. If WRF-Hydro is not  
731 coupled with sediment models, a domain-specific rainfall ID threshold trained with historic  
732 landslide inventory and triggering rainfall events (Tognacca et al., 2000; Gregoretti & Dalla  
733 Fontana, 2007, 2008) or a newly developed dimensionless discharge and Shields stress threshold  
734 (Tang et al., 2019; McGuire & Youberg, 2020) could provide guidance to help identify debris flow  
735 triggering time and location, which in turn may improve WRF-Hydro's debris flow initiation  
736 identification.

737  
738 In addition to constraining potential postfire debris flow volumes, WRF-Hydro's application in  
739 debris flow studies could be advanced via concerted engagement with uncertainties that are both  
740 external (meteorological forcing data) and internal (physical parameters) to the model. Previous  
741 studies have demonstrated that precipitation is often the largest source of uncertainty in hydrologic  
742 predictive models (Hapuarachchi et al., 2011; Alfieri et al., 2012). Engagement with precipitation  
743 forcing uncertainties in past, near-term, and future contexts could provide probabilistic nuance to  
744 natural hazard investigations. For example, (a) debris flow hindcast studies could use a diversity  
745 of precipitation datasets to isolate precipitation-derived debris flow uncertainties in historic events,  
746 (b) operational forecast efforts could utilize ensemble-based weather forecast data to inform  
747 likelihood statements in debris flow hazard assessments, and (c) probabilistic projections of debris  
748 flow likelihood in future climates could assess and partition uncertainties derived from emission  
749 pathway, model structure, or internal variability effects on meteorological forcings (Nikolopoulos  
750 et al., 2019; Hawkins & Sutton, 2009; Deser et al., 2020). Uncertainties internal to WRF-Hydro  
751 are also ripe for investigation. Probabilistic predictions crafted from an ensemble of perturbed  
752 model physics simulations have been used to predict rainfall-triggered shallow landslides (Raia et  
753 al., 2014; Canli et al., 2018; Zhang et al., 2018). Similar efforts using WRF-Hydro could target  
754 post-wildfire debris flows.

755  
756  
757  
758  
759  
760  
761  
762  
763  
764  
765  
766  
767  
768  
769  
770  
771  
772  
773  
774

Lastly, the above discussion of potential WRF-Hydro applications and advancements speaks to the adaptability and customization of this open-source numerical model. An additional layer of WRF-Hydro’s adaptability concerns its geographic focus. While we calibrate and use the model over a central California domain, the choice of geographic footprint is only limited by the availability of requisite initial and boundary conditions, environmental observations for calibration, and computational resources. For use in non-central California domains, we recommend calibration beginning with the default version of the model. Given the ecological and geological diversity of locations that experience wildfires and debris flows, it is likely that calibrations distinct from those reported here will be needed in different regions. For example, soil sealing effects, infiltration, and runoff in wetter and more vegetated locations, such as Oregon, USA, behave differently than those in central California (Palmer, 2022). As such, calibration of relevant model parameters (e.g., saturated hydraulic conductivities) should be based on a physics-informed approach that accounts for local environmental conditions and hydrologic behaviors. Indeed, given the ability to simulate large heterogeneous geographic domains, it is likely that different regions within a given domain may require different calibration schemes. As WRF-Hydro is fully distributed, spatially heterogeneous calibrations are non-problematic. This spatial adaptability may prove particularly helpful in post-wildfire debris flow hazard assessments when considering multiple generations of wildfires and variable degrees of burn scar severity and recovery.

775 **7 Conclusion**

776  
777  
778  
779  
780  
781  
782  
783  
784  
785  
786  
787  
788  
789  
790  
791  
792  
793

Here we augment WRF-Hydro to assess regional postfire debris flow susceptibility. Our methodology involves output of simulated overland flow data and alteration of the model’s representation of burn scars. In this application we have balanced the computational cost of a regional domain with our choice of resolved spatial resolution for terrain routing and overland flow calculations (100 m). However, WRF-Hydro has previously been applied to smaller domains at higher terrain routing resolutions (~30 m). Future work could assess the use of the model to study burn scar hydrology at finer spatial scales, should the application warrant and should underlying data at sufficient resolution exist. Other potential applications of our augmented model framework include alpine areas and steep hillslopes with sparse vegetation where runoff-generated debris flows dominate over landslide-initiated ones (Davies et al., 1992; Coe et al., 2003, 2008). Furthermore, our burn scar parameter changes are performed to Noah-MP, which is the core land surface component of the NCEP Global Forecast System (GFS) and Climate Forecast System (CFS), thus the findings presented herein, are likely to prove useful in the broader worlds of forecast meteorology and climate science. In addition, here WRF-Hydro is driven by historical precipitation and meteorological data, i.e., in hindcast mode. However, this modeling framework could also be employed to project hazards under future climatic conditions (e.g., Huang et al., 2020), or given its relatively low computational expense, in operational forecast mode. Indeed, modern ensemble-based meteorological forecasting could provide high spatiotemporal forcing

794 data with which disaster preparedness managers could probabilistically assess debris flow hazard  
795 potential, and issue advanced life and property saving warnings.

796  
797  
798

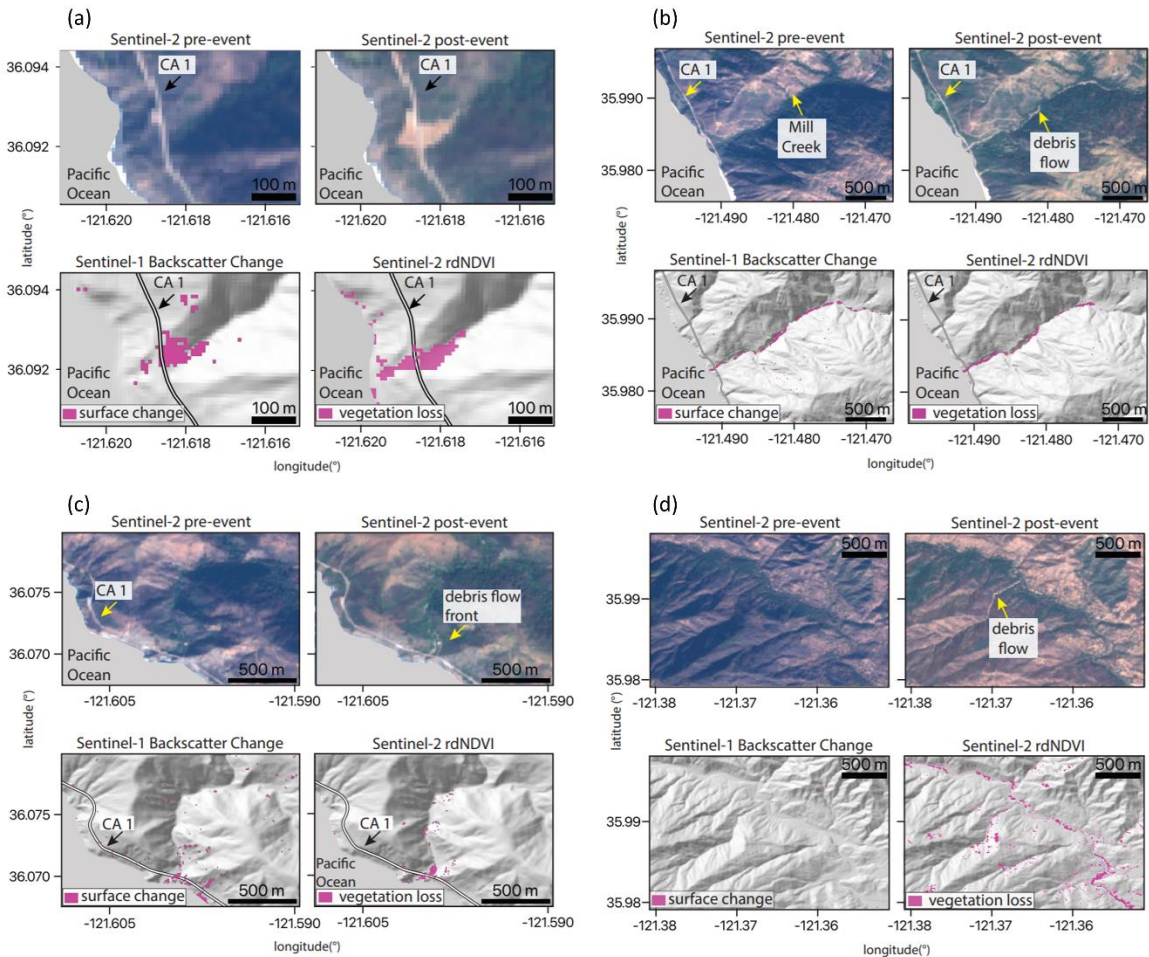
## 799 **Appendix A**

### 800 **Text A1. Multi-Radar/Multi-Sensor System (MRMS) radar-only precipitation estimate and** 801 **uncertainty**

802 MRMS is a precipitation product that covers the contiguous United States (CONUS) on 1-km grids.  
803 It combines precipitation estimates from sensors and observational networks (Zhang et al.,  
804 2011, 2014, 2016), and is produced at the National Centers for Environmental Prediction (NCEP)  
805 and distributed to National Weather Service forecast offices and other agencies. Input datasets  
806 used to produce MRMS include the U.S. Weather Surveillance Radar-1988 Doppler (WSR-88D)  
807 network and Canadian radar network, Parameter-elevation Regressions on Independent Slopes  
808 Model (PRISM; Daly et al. 1994, 2017), Hydrometeorological Automated Data System (HADS)  
809 gauge data with quality control (Qi et al., 2016), and outputs from numerical weather prediction  
810 models. There are four different MRMS quantitative precipitation estimates (QPE) products  
811 incorporating different input data or combinations: radar only, gauge only, gauge-adjusted radar,  
812 and Mountain Mapper. For our study period (i.e., January 1–31, 2021), only the radar-only QPE  
813 is currently available.

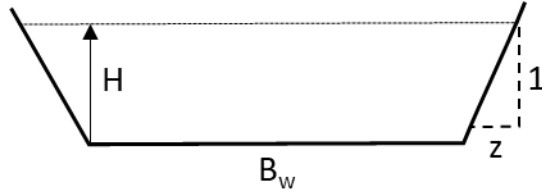
814  
815 We acknowledge that precipitation data has uncertainties. Use of different precipitation products  
816 may produce different results. A study comparing different gridded precipitation datasets including  
817 satellite-based precipitation data, gauge dataset, and multi-sensor products revealed large  
818 uncertainties in precipitation intensity (Bytheway et al., 2020). However, comparing different  
819 precipitation datasets to characterize uncertainties is beyond the scope of this study. MRMS  
820 provides gridded precipitation at high temporal (hourly) and spatial (1-km) resolutions, making it  
821 a useful tool to demonstrate the utility of WRF-Hydro in post-wildfire debris flow susceptibility  
822 assessments.





824  
 825  
 826  
 827  
 828  
 829  
 830  
 831  
 832  
 833  
 834  
 835

**Fig. B1** Optical- and SAR-based remote sensing data of four debris flows. Optical data from Sentinel-2 show pre- and post-debris flow imagery in real color. rdNDVI calculated from the Sentinel-2 data show a decrease in vegetation corresponding to debris flow locations. Sentinel-1 backscatter change shows the change in ground surface properties determined by calculating the log ratio of pre- and post-event SAR images. The pre-event, post-event satellite images, Sentinel-1 Backscatter, and Sentinel-2 rdNDVI change at (a) Rat Creek, (b) Mill Creek, (c) Big Creek, and (d) Nacimientos.



836

837 **Fig. B2** Schematic trapezoidal shape and related parameters of channels in WRF-Hydro.  $B_w$  is  
838 the channel bottom width (m),  $z$  is the channel side slope (m), and  $H$  is water elevation (m). The  
839 cross-sectional area of flow is calculated as  $(B_w + H z)H$ .

840

841 **Table B1** Parameters of trapezoidal channels in WRF-Hydro.

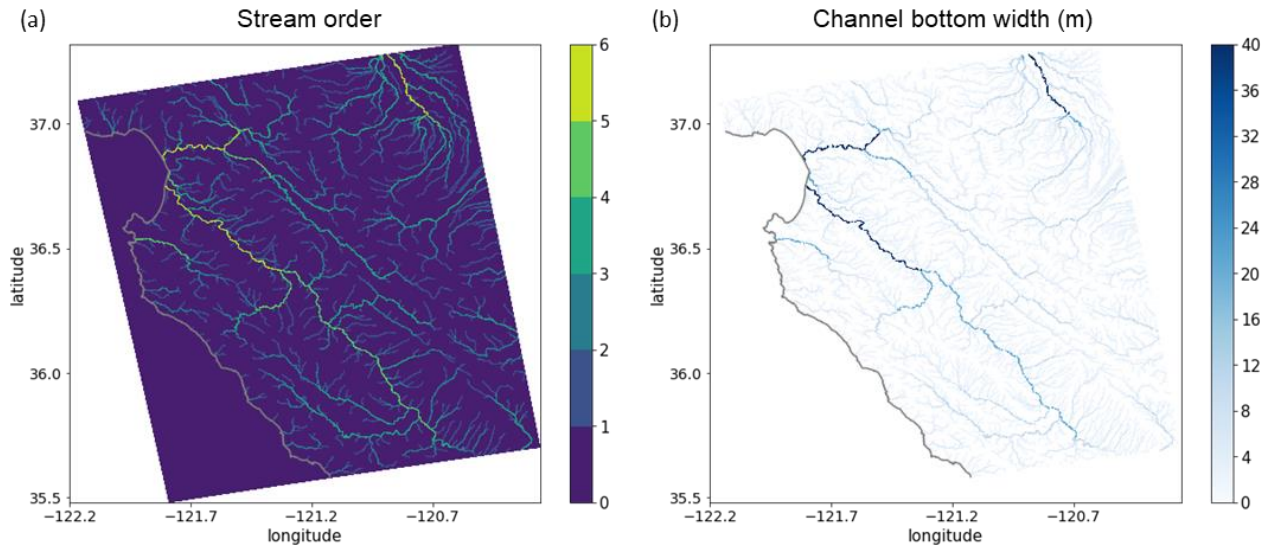
Stream order	Channel bottom width $B_w$ (m)	Channel side slope $z$ (m)	Manning's roughness coefficient $n$
1	1.5	3	0.33
2	3	1	0.21
3	5	0.5	0.09
4	10	0.18	0.06
5	20	0.05	0.04
6	40	0.05	0.03
7	60	0.05	0.02
8	70	0.05	0.02
9	80	0.05	0.01
10	100	0.05	0.01

842

843 **Table B1** Parameters of the trapezoidal channels in WRF-Hydro including channel bottom width  
 844  $B_w$  (m), channel side slope  $z$  (m), and Manning's roughness coefficient  $n$ .

845

846



847

848 **Fig. B3** (a) Stream order defined by the USGS 30-m DEM in our WRF-Hydro model domain  
 849 and (b) the channel bottom width (m) which is a function of stream order (Table B1).

850

851 *Table B2*

852 *MODIS IGBP 20-category land cover type and properties in Noah-MP LSM*

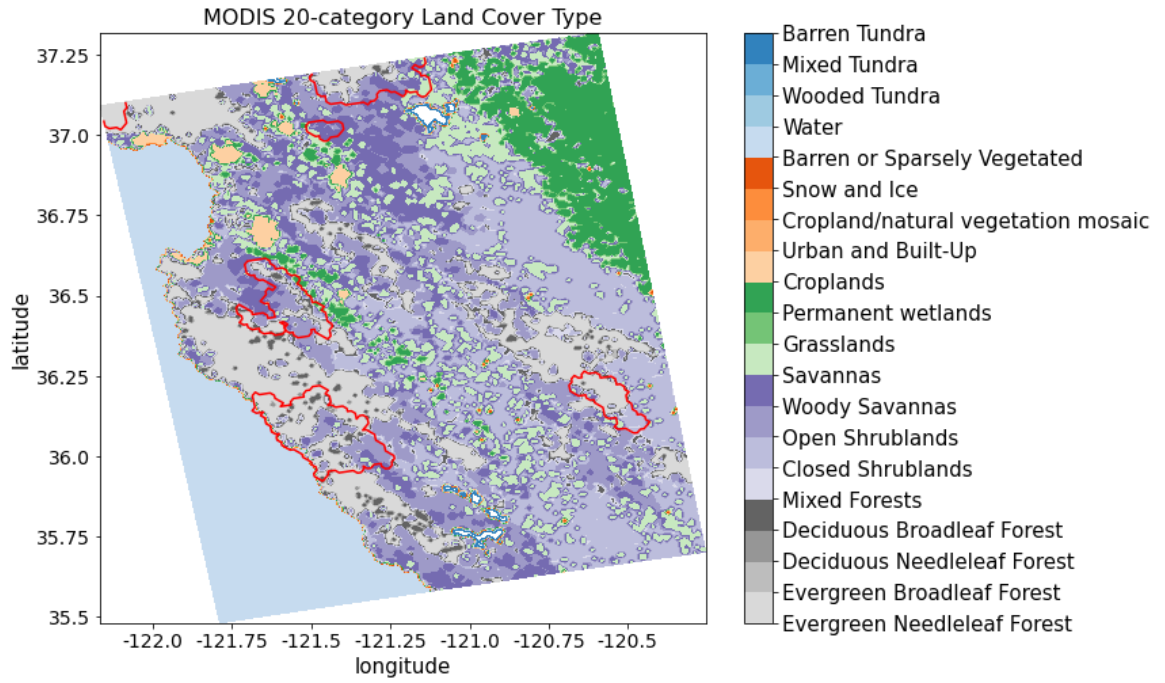
<b>Land cover code</b>	<b>Land cover type</b>	<b>Canopy height (m)</b>	<b>Max carboxylation rate at 25°C (<math>\mu\text{mol CO}_2/(\text{m}^2 \cdot \text{s})</math>)</b>	<b>Overland flow roughness</b>
1	Evergreen Needleleaf Forest	20	50	0.2
2	Evergreen Broadleaf Forest	20	60	0.2
3	Deciduous Needleleaf Forest	18	60	0.2
4	Deciduous Broadleaf Forest	16	60	0.2
5	Mixed Forests	16	55	0.2
6	Closed Shrublands	1.1	40	0.055
7	Open Shrublands	1.1	40	0.055
8	Woody Savannas	13	40	0.055
9	Savannas	10	40	0.055
10	Grasslands	1	40	0.055
11	Permanent wetlands	5	50	0.07
12	Croplands	2	80	0.035
13	Urban and Built-Up	15	0	0.025
14	Cropland/natural vegetation mosaic	1.5	60	0.035
15	Snow and Ice	0	0	0.01
16	Barren or Sparsely Vegetated	0	0	0.035
17	Water	0	0	0.005
18	Wooded Tundra	4	50	0.055
19	Mixed Tundra	2	50	0.055
20	Barren Tundra	0.5	50	0.055

853

854 **Table B2** MODIS IGBP 20-category land cover type and properties in Noah-MP LSM.

855

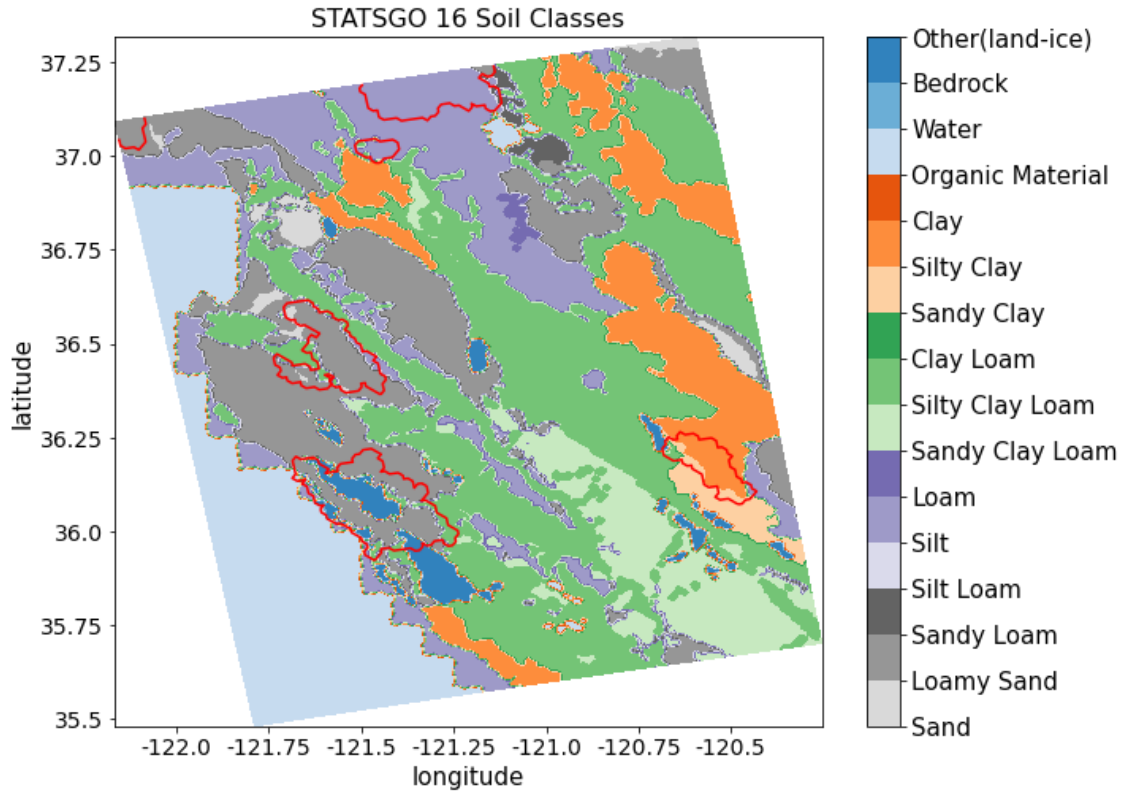
856



857 **Fig. B4** MODIS IGBP 20-category land cover type in the model domain. Red polylines are 2020  
 858 wildfire burn scar perimeters.

859

860



861 **Fig. B5** 1-km STATSGO data with 16 soil texture types. Red polylines are 2020 wildfire burn  
 862 scar perimeters.

863  
 864  
 865  
 866  
 867

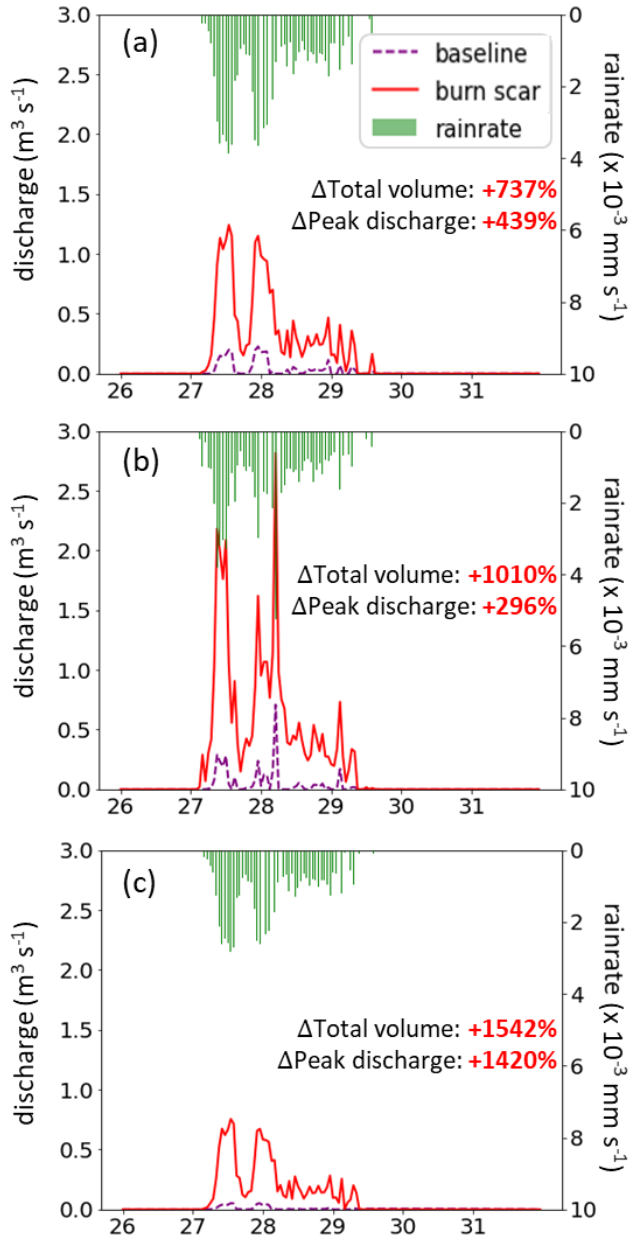
868 *Table B3*  
 869 *Default and calibrated soil parameters in WRF-Hydro*  
 870

Soil type	Default			After calibration		
	Grain size distribution index	Porosity	Saturated hydraulic conductivity (m s <sup>-1</sup> )	Grain size distribution index	Porosity	Saturated hydraulic conductivity (m s <sup>-1</sup> )
Sand	2.79	0.339	4.66E-5	2.51	0.315	1.5 x 10 <sup>-7</sup> m s <sup>-1</sup> for all the burn scars, and original values elsewhere.
Loamy sand	4.26	0.421	1.41E-5	3.83	0.392	
Sandy loam	4.74	0.434	5.23E-6	4.27	0.404	
Silt loam	5.33	0.476	2.81E-6	4.80	0.442	
Silt	3.86	0.484	2.18E-6	3.47	0.450	
Loam	5.25	0.439	3.38E-6	4.73	0.408	
Sandy clay loam	6.77	0.404	4.45E-6	6.09	0.376	
Silty clay loam	8.72	0.464	2.03E-6	7.85	0.432	
Clay loam	8.17	0.465	2.45E-6	7.35	0.432	
Sandy clay	10.73	0.406	7.22E-6	9.66	0.378	
Silty clay	10.39	0.468	1.34E-6	9.35	0.435	
Clay	11.55	0.468	9.74E-7	10.40	0.435	
Organic material	5.25	0.439	3.38E-6	4.73	0.408	
Water	0.00	1.00	0.00	0.00	1.00	
Bedrock	2.79	0.200	1.41E-4	2.51	0.186	
Other	4.26	0.421	1.41E-5	3.83	0.392	
Playa	11.55	0.468	9.74E-7	10.40	0.435	
Lava	2.79	0.200	1.41E-4	2.51	0.186	
White sand	2.79	0.339	4.66E-5	2.51	0.315	

871  
 872 **Table B3** Soil parameters in default and calibrated WRF-Hydro. Default soil parameters in WRF-  
 873 Hydro are adapted from the soil analysis by Cosby et al. (1984). Grain size distribution index and  
 874 soil porosity are altered from default values during the global soil moisture calibration. Saturated  
 875 hydraulic conductivity is altered from default values during the streamflow calibration.

876  
 877





878  
 879  
 880  
 881  
 882  
 883  
 884  
 885  
 886  
 887  
 888  
 889

**Fig. B6** WRF-Hydro simulated discharge time-series at four debris flow source areas. (a)–(c) MRMS precipitation (green bars) and simulated discharge time-series for January 26<sup>th</sup> 00:00 to 31<sup>st</sup> 23:00 at Mill Creek, Big Creek, and Nacimiento debris flow source areas (black circles in Fig. 7b–d) in baseline (purple dashed line) and burn scar simulation (red line).

890 *Table B4*

891 *The total runoff volume, peak discharge, and peak timing at debris-flow source areas*

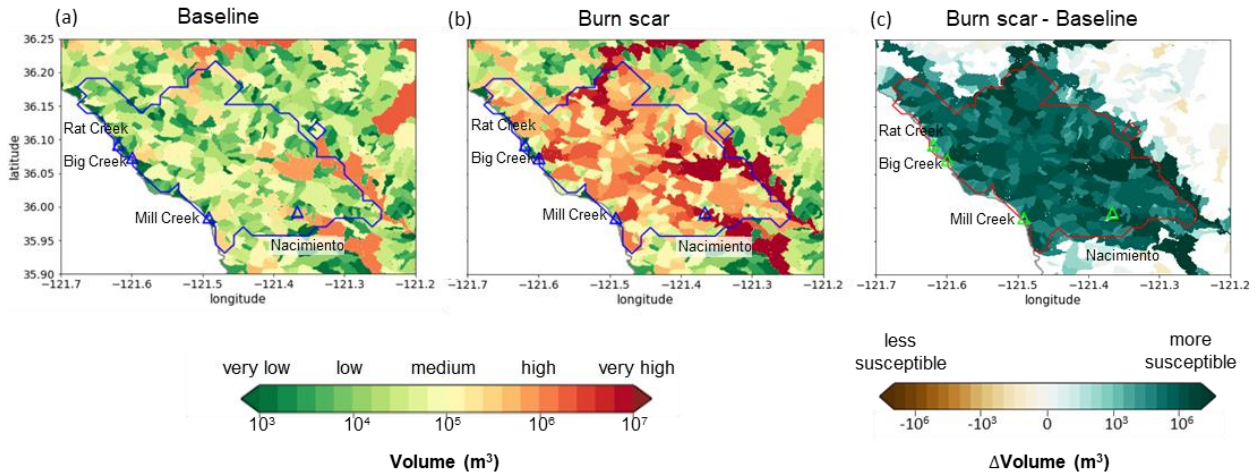
Site name	Baseline simulation			Burn scar simulation		
	Total volume (m <sup>3</sup> )	Peak discharge (m <sup>3</sup> s <sup>-1</sup> )	Peak timing	Total volume (m <sup>3</sup> )	Peak discharge (m <sup>3</sup> s <sup>-1</sup> )	Peak timing
Mill Creek	10,023	0.23	27 <sup>th</sup> 23:00	83,853 (+737%)	1.24 (+439%)	27 <sup>th</sup> 13:00
Big Creek	11,611	0.71	28 <sup>th</sup> 05:00	128,879 (+1010%)	2.81 (+296%)	28 <sup>th</sup> 05:00
Nacimiento	3,031	0.05	27 <sup>th</sup> 13:00	49,792 (+1542%)	0.76 (+1420%)	27 <sup>th</sup> 13:00

892  
893 **Table B4** The total runoff volume, peak discharge, and peak timing in the baseline and burn scar  
894 simulations from January 27<sup>th</sup> 00:00 to 31<sup>st</sup> 23:00 at source areas of Rat Creek, Mill Creek, Big  
895 Creek, and Nacimiento debris flows (black circles in Fig. 7b–d). The percent change of the total  
896 volume and peak discharge in the burn scar simulation relative to the baseline simulation are shown  
897 in parentheses.

898

899

## Non-normalized catchment postfire debris flow susceptibility



900

901

902 **Fig. B7** Discharge volume-based runoff-generated debris flow susceptibility at catchment level in  
 903 the (a) baseline simulation, (b) burn scar simulation, and (c) the difference between the burn scar  
 904 and baseline simulations. For each catchment, the susceptibility is assessed by computing the total  
 905 discharge volume at the catchment outlet from January 27<sup>th</sup> 00:00 to 28<sup>th</sup> 12:00.

906

### 907 Data availability statement

908 The NLDAS-2 reanalysis forcing data is publicly available at NASA GES DISC:  
 909 <https://disc.gsfc.nasa.gov/datasets?keywords=NLDAS>. A detailed description can be found at  
 910 <https://ldas.gsfc.nasa.gov/nldas/v2/forcing>. The MRMS radar-only precipitation estimate is  
 911 publicly available at: <https://mtarchive.geol.iastate.edu/>. A description can be found at  
 912 <https://www.nssl.noaa.gov/projects/mrms/>. The PSL in-situ soil moisture data is publicly available  
 913 at: <https://psl.noaa.gov/data/obs/datadisplay/>. The USGS streamflow is publicly available at:  
 914 <https://waterdata.usgs.gov/nwis/>. The wildfire perimeter shapefiles are downloadable at:  
 915 <https://data-nifc.opendata.arcgis.com/search?collection=Dataset>. The remote sensing data used in  
 916 this manuscript were provided by the European Space Agency (ESA) Copernicus program and  
 917 accessed on Google Earth Engine (<https://code.earthengine.google.com>). All processed data  
 918 required to reproduce the results of this study are archived on Zenodo at  
 919 <http://doi.org/10.5281/zenodo.5544083>.

920 **Code availability statement**

921 The modified WRF-Hydro Fortran code and instructions to output the overland flow at terrain  
922 routing grid can be downloaded at <https://github.com/NU-CCRG/Modified-WRF-Hydro>.

923 HazMapper v1.0 is available at <https://hazmapper.org/>. The SAR backscatter change method code  
924 is available at [https://github.com/MongHanHuang/GEE\\_SAR\\_landslide\\_detection](https://github.com/MongHanHuang/GEE_SAR_landslide_detection).

925 **Author contribution**

926 Conceptualization: CL, ALH, & DEH; Simulation and model analysis: CL; JW & WY model  
927 methodological development. Remote sensing analysis: ALH; Field Observations: NJF; GIS  
928 assistance: YX; Funding acquisition: GB & DH; CL wrote the original draft and all authors  
929 reviewed and edited the manuscript.

930 **Competing interests**

931 The authors declare that they have no conflict of interest.

932 **Acknowledgments**

933 C.L., A.L.H., J.W., X.L., G.B., and D.E.H. acknowledge support from NSF PREEVENTS  
934 #1848683. We acknowledge high-performance computing support from Cheyenne  
935 (doi:10.5065/D6RX99HX) provided by NCAR's Computational and Information Systems  
936 Laboratory, sponsored by the National Science Foundation. We thank P. Santi, an anonymous  
937 reviewer, and the editor for formal reviews, and F. K. Rengers for informal comments.  
938

939

940 **References**

- 941 Alfieri L., Salamon P., Pappenberger F., Wetterhall F., Thielen J. (2012). Operational early warning systems for  
942 water-related hazards in Europe *Environmental Science & Policy* 21:35-49  
943 doi:<https://doi.org/10.1016/j.envsci.2012.01.008>
- 944 Anderson, H. W., Hoover, M. D., & Reinhart, K. G. (1976). *Forests and water: effects of forest management on*  
945 *floods, sedimentation, and water supply* (Vol. 18): Department of Agriculture, Forest Service, Pacific  
946 Southwest Forest and Range Experiment Station, Berkeley, CA.
- 947 Andersson, J. C. M., Arheimer, B., Traoré, F., Gustafsson, D., & Ali, A. (2017). Process refinements improve a  
948 hydrological model concept applied to the Niger River basin. *Hydrological Processes*, 31(25), 4540-  
949 4554. doi:<https://doi.org/10.1002/hyp.11376>
- 950 Arattano, M., & Franzi, L. (2010). On the application of kinematic models to simulate the diffusive processes of  
951 debris flows. *Nat. Hazards Earth Syst. Sci.*, 10(8), 1689-1695. doi:10.5194/nhess-10-1689-2010

952 Arattano, M., & Savage, W.Z. (1994). Modelling debris flows as kinematic waves. *Bulletin of the International*  
953 *Association of Engineering Geology* 49, 3–13. <https://doi.org/10.1007/BF02594995>

954 Bart, R. (2016). A regional estimate of postfire streamflow change in California. *Water Resources Research*, 52,  
955 n/a-n/a. doi:10.1002/2014WR016553

956 Bart, R., & Hope, A. (2010). Streamflow response to fire in large catchments of a Mediterranean-climate region  
957 using paired-catchment experiments. *Journal of Hydrology*, 388, 370-378.  
958 doi:10.1016/j.jhydrol.2010.05.016

959 Brabb E.E. (1985) Innovative approaches to landslide hazard and risk mapping. In: *International Landslide*  
960 *Symposium Proceedings*, Toronto, Canada. pp 17-22

961 Bisson M., Favalli M., Fornaciai A., Mazzarini F., Isola I., Zanchetta G., & Pareschi M.T. (2005). A rapid method  
962 to assess fire-related debris flow hazard in the Mediterranean region: An example from Sicily (southern  
963 Italy) *International Journal of Applied Earth Observation and Geoinformation* 7:217-231  
964 doi:<https://doi.org/10.1016/j.jag.2005.04.003>

965 Bitew, M. M., & Gebremichael, M. (2011). Assessment of satellite rainfall products for streamflow simulation  
966 in medium watersheds of the Ethiopian highlands. *Hydrol. Earth Syst. Sci.*, 15(4), 1147-1155.  
967 doi:10.5194/hess-15-1147-2011

968 Brown, E.K., Wang, J., & Feng, Y. (2020). U.S. wildfire potential: a historical view and future projection using  
969 high-resolution climate data. *Environmental Research Letters*. 16, 034060

970 Brunkal, H., & Santi, P. M. (2016). Exploration of design parameters for a dewatering structure for debris flow  
971 mitigation. 208, 81-92.

972 Bytheway, J. L., Hughes, M., Mahoney, K., & Cifelli, R. (2020). On the Uncertainty of High-Resolution Hourly  
973 Quantitative Precipitation Estimates in California, *Journal of Hydrometeorology*, 21(5), 865-879.  
974 Retrieved Oct 25, 2021, from [https://journals.ametsoc.org/view/journals/hydr/21/5/jhm-d-19-](https://journals.ametsoc.org/view/journals/hydr/21/5/jhm-d-19-0160.1.xml)  
975 [0160.1.xml](https://journals.ametsoc.org/view/journals/hydr/21/5/jhm-d-19-0160.1.xml)

976 Canfield, H. E., Goodrich, D. C., & Burns, I. S. (2005). Selection of parameters values to model post-fire runoff  
977 and sediment transport at the watershed scale in southwestern forests. In *Managing watersheds for*  
978 *human and natural impacts: engineering, ecological, and economic challenges* (pp. 1-12).

979 Canli E., Mergili M., Thiebes B., & Glade T. (2018) Probabilistic landslide ensemble prediction systems: lessons  
980 to be learned from hydrology *Nat Hazards Earth Syst Sci* 18:2183-2202 doi:10.5194/nhess-18-2183-  
981 2018

982 Cannon, S.H., Kirkham R.M., & Paise M., (2001). Wildfire-related debris-flow initiation processes, Storm King  
983 Mountain, Colorado. *Geomorphology*, v.39, n. 3-4, 171-188

984 Cannon, S. H., Gartner, J. E., Parrett, C., & Parise, M. (2003). Wildfire-related debris-flow generation through  
985 episodic progressive sediment-bulking processes, western USA. *Debris-Flow Hazards Mitigation:*  
986 *Mechanics, Prediction, and Assessment*. Millpress, Rotterdam, pp. 71-82.

987 Cannon, S. H., Gartner, J., Wilson, R., Bowers, J., & Laber, J. (2008). Storm Rainfall Conditions for Floods and  
988 Debris Flows from Recently Burned Basins in Southwestern Colorado and Southern California.  
989 *Geomorphology*, 96, 250-269. Doi:10.1016/j.geomorph.2007.03.019

990 Cannon, S. H., & DeGraff, J. (2009). The increasing wildfire and postfire debris flow threat in western USA,  
991 and implications for consequences of climate change. In *Landslides—disaster risk reduction* (pp. 177-  
992 190): Springer.

993 Cannon, S. H., Gartner, J. E., Rupert, M. G., Michael, J. A., Rea, A. H., & Parrett, C. (2010). Predicting the  
994 probability and volume of postwildfire debris flows in the intermountain western United States. *GSA*  
995 *Bulletin*, 122(1-2), 127-144. Doi:10.1130/B26459.1

996 Cannon, S. H., Boldt, E. M., Laber, J. L., Kean, J. W., & Staley, D. M. J. N. H. (2011). Rainfall intensity–  
997 duration thresholds for postfire debris flow emergency-response planning. 59(1), 209-236.

- 998 Cavagnaro, D. et al. (2021) Variability in hydrologic response to rainfall across a burn scar: observations from  
 999 the Dolan Fire, California. AGU abstract.  
 1000 <https://agu.confex.com/agu/fm21/meetingapp.cgi/Paper/921613>
- 1001 Cerdà, A. (1998). Changes in overland flow and infiltration after a rangeland fire in a Mediterranean scrubland.  
 1002 *Hydrological Processes*, 12(7), 1031-1042. Doi:[https://doi.org/10.1002/\(SICI\)1099-1085\(19980615\)12:7<1031::AID-HYP636>3.0.CO;2-V](https://doi.org/10.1002/(SICI)1099-1085(19980615)12:7<1031::AID-HYP636>3.0.CO;2-V)
- 1003  
 1004 Chen, F., & Dudhia, J. (2001). Coupling an Advanced Land Surface–Hydrology Model with the Penn State–  
 1005 NCAR MM5 Modeling System. Part I: Model Implementation and Sensitivity, *Monthly Weather*  
 1006 *Review*, 129(4), 569-585. Retrieved Oct 24, 2021, from  
 1007 [https://journals.ametsoc.org/view/journals/mwre/129/4/1520-0493\\_2001\\_129\\_0569\\_caalsh\\_2.0.co\\_2.xml](https://journals.ametsoc.org/view/journals/mwre/129/4/1520-0493_2001_129_0569_caalsh_2.0.co_2.xml)
- 1008  
 1009 Chen, L., Berli, M., & Chief, K. (2013). Examining Modeling Approaches for the Rainfall-Runoff Process in  
 1010 Wildfire-Affected Watersheds: Using San Dimas Experimental Forest. *JAWRA Journal of the*  
 1011 *American Water Resources Association*, 49(4), 851-866. Doi:<https://doi.org/10.1111/jawr.12043>
- 1012 Claessens L., Schoorl, J.M., & Veldkamp, A. (2007) Modelling the location of shallow landslides and their  
 1013 effects on landscape dynamics in large watersheds: An application for Northern New Zealand  
 1014 *Geomorphology* 87:16-27 doi:<https://doi.org/10.1016/j.geomorph.2006.06.039>
- 1015 Crosta G. B., & Frattini P. (2003) Distributed modelling of shallow landslides triggered by intense rainfall. *Nat*  
 1016 *Hazards Earth Syst Sci* 3:81-93 doi:10.5194/nhess-3-81-2003
- 1017 Cui, Y., Cheng, D., & Chan, D. (2018). Investigation of post-fire debris flows in Montecito. *ISPRS International*  
 1018 *Journal of Geo-Information*, 8(1), 5.
- 1019 Coe, J., Godt, J., Parise, M., & Moscariello, A. (2003). Estimating debris flow probability using fan stratigraphy,  
 1020 historic records, and drainage-basin morphology, Interstate 70 highway corridor, central Colorado, USA.  
 1021 Paper presented at the Debris flow Hazards Mitigation: Mechanics, Prediction, and Assessment, edited  
 1022 by: Rickenmann, D. and Cheng, Ch., *Proceedings 3<sup>rd</sup> International DFHM Conference*, Davos,  
 1023 Switzerland.
- 1024 Coe, J. A., Kinner, D. A., & Godt, J. W. J. G. (2008). Initiation conditions for debris flows generated by runoff  
 1025 at Chalk Cliffs, central Colorado. 96(3-4), 270-297.
- 1026 Cosby, B. J., Hornberger, G. M., Clapp, R. B., & Ginn, T. R. (1984). A Statistical Exploration of the  
 1027 Relationships of Soil Moisture Characteristics to the Physical Properties of Soils. *Water Resources*  
 1028 *Research*, 20(6), 682-690. Doi:<https://doi.org/10.1029/WR020i006p00682>
- 1029 Cydzik, K., & Hogue, T. S. (2009). Modeling postfire response and recovery using the hydrologic engineering  
 1030 center hydrologic modeling system (HEC-HMS) 1. *JAWRA Journal of the American Water Resources*  
 1031 *Association*, 45(3), 702-714.
- 1032 Dahal, R.K., Hasegawa, S., Nonomura, A., Yamanaka, M., Dhakal, S., Paudyal, P. (2008) Predictive modelling  
 1033 of rainfall-induced landslide hazard in the Lesser Himalaya of Nepal based on weights-of-evidence  
 1034 *Geomorphology* 102:496-510 doi:<https://doi.org/10.1016/j.geomorph.2008.05.041>
- 1035 Daly, C., R. P. Neilson, & D. L. Phillips. (1994). A statistical-topographic model for mapping climatological  
 1036 precipitation over mountainous terrain. *J. Appl. Meteor.*, 33, 140–1
- 1037 Daly, C., M. E. Slater, J. A. Roberti, S. H. Laseter, & L. W. Swift Jr. (2017). High-resolution precipitation  
 1038 mapping in a mountainous watershed; Ground truth for evaluating uncertainty in a national precipitation  
 1039 dataset. *Int. J. Climatol.*, 37, 124–137, <https://doi.org/10.1002/joc.4986>.
- 1040 Davies, T., Phillips, C., Pearce, A., & Zhang, X. J. I. P. (1992). Debris flow behaviour—an integrated overview.  
 1041 *209(21)*, 225.

1042 Dekker, L. W., & Ritsema, C. J. (1994). How water moves in a water repellent sandy soil: 1. Potential and actual  
1043 water repellency. *Water Resources Research*, 30(9), 2507-2517.  
1044 Doi:<https://doi.org/10.1029/94WR00749>

1045 Deser, C. et al. (2020) Insights from Earth system model initial-condition large ensembles and future prospects  
1046 *Nature Climate Change* 10:277-286 doi:10.1038/s41558-020-0731-2

1047 Di Cristo, C., Iervolino, M., Moramarco, T., & Vacca, A. (2021). Applicability of Diffusive model for mud-  
1048 flows: An unsteady analysis. *Journal of Hydrology*, 600, 126512.  
1049 Doi:<https://doi.org/10.1016/j.jhydrol.2021.126512>

1050 Doerr, S. H., & Thomas, A. (2000). The role of soil moisture in controlling water repellency: New evidence  
1051 from forest soils in Portugal. *Journal of Hydrology*, 231-232, 134-147. Doi:10.1016/S0022-  
1052 1694(00)00190-6

1053 Flannigan, M., Cantin, A. S., De Groot, W. J., Wotton, M., Newbery, A., & Gowman, L. M. (2013). Global  
1054 wildland fire season severity in the 21st century. *Forest Ecology and Management*, 294, 54-61.

1055 Friedel, M.J. (2011a). A data-driven approach for modeling post-fire debris-flow volumes and their uncertainty  
1056 *Environmental Modelling & Software* 26:1583-1598 doi:<https://doi.org/10.1016/j.envsoft.2011.07.014>

1057 Friedel, M.J. (2011b) Modeling hydrologic and geomorphic hazards across post-fire landscapes using a self-  
1058 organizing map approach *Environmental Modelling & Software* 26:1660-1674  
1059 doi:<https://doi.org/10.1016/j.envsoft.2011.07.001>

1060 Gartner, J. E., Cannon, S. H., & Santi, P. M. (2014). Empirical models for predicting volumes of sediment  
1061 deposited by debris flows and sediment-laden floods in the transverse ranges of southern California.  
1062 *Engineering Geology*, 176, 45-56. doi:<https://doi.org/10.1016/j.enggeo.2014.04.008>

1063 George, D. L., & Iverson, R. M. (2014). A depth-averaged debris flow model that includes the effects of evolving  
1064 dilatancy. II. Numerical predictions and experimental tests. *Proceedings of the Royal Society A: Mathematical, Physical and Engineering Sciences*, 470(2170), 20130820. doi:10.1098/rspa.2013.0820

1065 Gochis, D. J., & Chen, F. (2003). Hydrological Enhancements to the Community Noah Land Surface Model (No.  
1066 NCAR/TN-454+STR). University Corporation for Atmospheric Research. doi:10.5065/D60P0X00

1067 Goodrich, D., Burns, I., Unkrich, C., Semmens, D., Guertin, D., Hernandez, M., . . . Levick, L. (2012).  
1068 KINEROS2/AGWA: model use, calibration, and validation. *Transactions of the ASABE*, 55, 1561-  
1069 1574. doi:10.13031/2013.42264

1070 Goss, M., Swain, D. L., Abatzoglou, J. T., Sarhadi, A., Kolden, C. A., Williams, A. P., & Diffenbaugh, N. S.  
1071 (2020). Climate change is increasing the likelihood of extreme autumn wildfire conditions across  
1072 California. *Environmental Research Letters*, 15(9), 094016. doi:10.1088/1748-9326/ab83a7

1073 Gregoretti, C., & Dalla Fontana, G. (2007). Rainfall threshold for the initiation of debris flows by channel-bed  
1074 failure in the Dolomites. *Debris-Flow Hazards Mitigation: Mechanics, Prediction, and Assessment*, 11-  
1075 22.

1076 Gregoretti, C., & Dalla Fontana, G. (2008). The triggering of debris flow due to channel-bed failure in some  
1077 alpine headwater basins of the Dolomites: analyses of critical runoff. *Hydrological Processes*, 22(13),  
1078 2248-2263. doi:<https://doi.org/10.1002/hyp.6821>

1079 Gupta, H. V., Kling, H., Yilmaz, K. K., & Martinez, G. F. (2009). Decomposition of the mean squared error and  
1080 NSE performance criteria: Implications for improving hydrological modelling. *Journal of Hydrology*,  
1081 377(1), 80-91. doi:<https://doi.org/10.1016/j.jhydrol.2009.08.003>

1082 Guzzetti, F., Reichenbach, P., Cardinali, M., Galli, M., & Ardizzone, F. J. G. (2005) Probabilistic landslide  
1083 hazard assessment at the basin scale *72:272-299*

1084 Handwerker, A. L., Huang, M.-H., Jones, S. Y., Amatya, P., Kerner, H. R., and Kirschbaum, D. B. (2022)  
1085 Generating landslide density heatmaps for rapid detection using open-access satellite radar data in  
1086 Google Earth Engine, *Nat. Hazards Earth Syst. Sci. Discuss.* doi:10.5194/nhess-2021-283

1087

1088 Hapuarachchi, H.A.P., Wang, Q.J., & Pagano, T.C. (2011) A review of advances in flash flood forecasting.  
1089 Hydrological processes, 25:2771-2784 doi:<https://doi.org/10.1002/hyp.8040>

1090 Hawkins, E., Sutton, R. (2009) The Potential to Narrow Uncertainty in Regional Climate Predictions Bull Amer  
1091 Meteor Soc 90:1095-1108 doi:10.1175/2009BAMS2607.1

1092 Huang, X., Swain, D. L., & Hall, A. D. (2020). Future precipitation increase from very high resolution ensemble  
1093 downscaling of extreme atmospheric river storms in California. 6(29), eaba1323.  
1094 doi:10.1126/sciadv.aba1323 %J Science Advances

1095 Ice, G. G., Neary, D. G., & Adams, P. W. (2004). Effects of Wildfire on Soils and Watershed Processes. Journal  
1096 of Forestry, 102(6), 16-20. doi:10.1093/jof/102.6.16

1097 Iverson, R. M., & George, D. L. (2014). A depth-averaged debris flow model that includes the effects of evolving  
1098 dilatancy. I. Physical basis. Proceedings of the Royal Society A: Mathematical, Physical and  
1099 Engineering Sciences, 470(2170), 20130819. doi:10.1098/rspa.2013.0819

1100 Jolly, W. M., Cochrane, M. A., Freeborn, P. H., Holden, Z. A., Brown, T. J., Williamson, G. J., & Bowman, D.  
1101 M. J. S. (2015). Climate-induced variations in global wildfire danger from 1979 to 2013. Nature  
1102 Communications, 6(1), 7537. doi:10.1038/ncomms8537

1103 Julien, P. Y., Saghafian, B., & Ogden, F. L. (1995). RASTER-BASED HYDROLOGIC MODELING OF  
1104 SPATIALLY-VARIED SURFACE RUNOFF1. JAWRA Journal of the American Water Resources  
1105 Association, 31(3), 523-536. doi:<https://doi.org/10.1111/j.1752-1688.1995.tb04039.x>

1106 Kean, J. W., Staley, D. M., & Cannon, S. H. (2011). In situ measurements of postfire debris flows in southern  
1107 California: Comparisons of the timing and magnitude of 24 debris flow events with rainfall and soil  
1108 moisture conditions. Journal of Geophysical Research F: Earth Surface, 116(4).  
1109 doi:10.1029/2011JF002005

1110 Kean, J. W., McCoy, S. W., Tucker, G. E., Staley, D. M., & Coe, J. A. (2013). Runoff-generated debris flows:  
1111 Observations and modeling of surge initiation, magnitude, and frequency. Journal of Geophysical  
1112 Research: Earth Surface, 118(4), 2190-2207. doi:<https://doi.org/10.1002/jgrf.20148>

1113 Kean, J. W., & Staley, D. M. (2021). Forecasting the Frequency and Magnitude of Postfire Debris Flows Across  
1114 Southern California. Earth's Future, 9(3), e2020EF001735. doi:<https://doi.org/10.1029/2020EF001735>

1115 Kinoshita, A. M., & Hogue, T. S. (2015). Increased dry season water yield in burned watersheds in Southern  
1116 California. Environmental Research Letters, 10(1), 014003. doi:10.1088/1748-9326/10/1/014003

1117 Kling, H., Fuchs, M., & Paulin, M. (2012). Runoff conditions in the upper Danube basin under an ensemble of  
1118 climate change scenarios. Journal of Hydrology, 424-425, 264-277.  
1119 doi:<https://doi.org/10.1016/j.jhydrol.2012.01.011>

1120 Larsen, I., MacDonald, L., Brown, E., Rough, D., Welsh, M., Pietraszek, J., . . . Schaffrath, K. (2009). Causes  
1121 of Postfire Runoff and Erosion: Water Repellency, Cover, or Soil Sealing? Soil Science Society of  
1122 America Journal - SSSAJ, 73. doi:10.2136/sssaj2007.0432

1123 Lahmers, T. M., Gupta, H., Castro, C. L., Gochis, D. J., Yates, D., Dugger, A., . . . Hazenberg, P. J. J. o. H.  
1124 (2019). Enhancing the structure of the WRF-Hydro hydrologic model for semiarid environments. 20(4),  
1125 691-714.

1126 Lahmers, T. M., Castro, C. L., & Hazenberg, P. (2020). Effects of Lateral Flow on the Convective Environment  
1127 in a Coupled Hydrometeorological Modeling System in a Semiarid Environment, Journal of  
1128 Hydrometeorology, 21(4), 615-642. Retrieved Sep 29, 2021, from  
1129 <https://journals.ametsoc.org/view/journals/hydr/21/4/jhm-d-19-0100.1.xml>

1130 MacDonald, L. H., & Huffman, E. L. (2004). Postfire soil water repellency: Persistence and soil moisture  
1131 thresholds. Soil Science Society of America Journal, 68, 1729-1734.

1132 Martin, D., & Moody, J. (2001). Comparison of Soil Infiltration Rates in Burned and Unburned Mountainous  
1133 Watersheds. Hydrological Processes, 15, 2893-2903. doi:10.1002/hyp.380



- 1134 McGuire, L. A., J. W. Kean, D. M. Staley, F. K. Rengers, and T. A. Wasklewicz (2016), Constraining the relative  
1135 importance of raindrop- and flow-driven sediment transport mechanisms in postwildfire environments  
1136 and implications for recovery time scales, *J. Geophys. Res. Earth Surf.*, 121, 2211– 2237,  
1137 doi:10.1002/2016JF003867
- 1138 McGuire, L. A., Rengers, F. K., Kean, J. W., & Staley, D. M. (2017). Debris flow initiation by runoff in a  
1139 recently burned basin: Is grain-by-grain sediment bulking or en masse failure to blame? *Geophysical*  
1140 *Research Letters*, 44(14), 7310-7319. doi:https://doi.org/10.1002/2017GL074243
- 1141 McGuire, L. A., & Youberg, A. M. (2020). What drives spatial variability in rainfall intensity-duration thresholds  
1142 for post-wildfire debris flows? Insights from the 2018 Buzzard Fire, NM, USA. *Landslides*, 17(10),  
1143 2385-2399. doi:10.1007/s10346-020-01470-y
- 1144 McMichael, C. E., & Hope, A. S. (2007). Predicting streamflow response to fire-induced landcover change:  
1145 implications of parameter uncertainty in the MIKE SHE model. *J Environ Manage*, 84(3), 245-256.  
1146 doi:10.1016/j.jenvman.2006.06.003
- 1147 Meixner, T., & Wohlgemuth, P. M. (2003). Climate variability, fire, vegetation recovery, and watershed  
1148 hydrology. In *Proceedings of the First Interagency Conference on Research in the Watersheds*, Benson,  
1149 Arizona (pp. 651-656).
- 1150 Meyer, G. A., & Wells, S. G. (1997). Fire-related sedimentation events on alluvial fans, Yellowstone National  
1151 Park, U.S.A. *Journal of Sedimentary Research*, 67(5), 776-791. doi:10.1306/D426863A-2B26-11D7-  
1152 8648000102C1865D
- 1153 Miller, D. A., & White, R. A. (1998). A Conterminous United States Multilayer Soil Characteristics Dataset for  
1154 Regional Climate and Hydrology Modeling, *Earth Interactions*, 2(2), 1-26. Retrieved Sep 27, 2021, from  
1155 https://journals.ametsoc.org/view/journals/eint/2/2/1087-3562\_1998\_002\_0001\_acusms\_2.3.co\_2.xml
- 1156 Mitsopoulos, I. D., & Mironidis, D. (2006). Assessment of post fire debris flow potential in a Mediterranean  
1157 type ecosystem. *WIT Transactions on Ecology and the Environment*, 90.
- 1158 Moody, J. A., Shakesby, R. A., Robichaud, P. R., Cannon, S. H., & Martin, D. A. (2013). Current research issues  
1159 related to post-wildfire runoff and erosion processes. *Earth-Science Reviews*, 122, 10-37.  
1160 doi:https://doi.org/10.1016/j.earscirev.2013.03.004
- 1161 Moriasi, D. N., Arnold, J. G., Van Liew, M. W., Bingner, R. L., Harmel, R. D., & Veith, T. L. (2007). Model  
1162 evaluation guidelines for systematic quantification of accuracy in watershed simulations. *Transactions*  
1163 *of the ASABE*, 50(3), 885-900.
- 1164 Nash, J. E., & Sutcliffe, J. V. (1970). River flow forecasting through conceptual models part I — A discussion  
1165 of principles. *Journal of Hydrology*, 10(3), 282-290. doi:https://doi.org/10.1016/0022-1694(70)90255-  
1166 6
- 1167 Neary, D. G., Gottfried, G. J., & Ffolliott, P. F. (2003). Post-wildfire watershed flood responses. In *Proceedings*  
1168 *of the 2nd International Fire Ecology Conference*, Orlando, Florida (pp. 16-20).
- 1169 Nikolopoulos, E.I., Destro, E., Bhuiyan, M.A.E, Borga, M., & Anagnostou, E.N. (2018). Evaluation of predictive  
1170 models for postfire debris flow occurrence in the western United States *Nat Hazards Earth Syst Sci*  
1171 18:2331-2343 doi:10.5194/nhess-18-2331-2018
- 1172 Nikolopoulos, E.I., Schwartz, C., Zhang, X, & Anagnostou, E.N. (2019) Rainfall estimation uncertainty and  
1173 early warning procedures for post-fire debris flows. In: *Geophysical Research Abstracts*.
- 1174 Niu, G-Y et al. (2011) The community Noah land surface model with multiparameterization options (Noah-MP):  
1175 1. Model description and evaluation with local-scale measurements *J Geophys Res Atm* 116  
1176 doi:https://doi.org/10.1029/2010JD015139
- 1177 Nyman, P., Smith, H.G., Sherwin, C.B., Langhans, C., Lane, P.N. J., & Sheridan, G.J. (2015). Predicting  
1178 sediment delivery from debris flows after wildfire. *Geomorphology*, 250, 173-186.  
1179 doi:https://doi.org/10.1016/j.geomorph.2015.08.023

1180 Oakley, N.S. (2021). A warming climate adds complexity to postfire hydrologic hazard planning. *Earth's Future*,  
1181 9, e2021EF002149. <https://doi.org/10.1029/2021EF002149>

1182 Ogden, F.L. (1997). *CASC2D reference manual*. Department of Civil & Environmental Engineering, University  
1183 of Connecticut, Storrs.

1184 Palmer, J. (2022). The devastating mudslides that follow forest fires. *Nature*.  
1185 <https://www.nature.com/articles/d41586-022-00028-3>.

1186 Parise, M., & Cannon, S.H. (2008) The effects of wildfires on erosion and debris-flow generation in  
1187 Mediterranean climatic areas: a first database. *Proceedings of 1<sup>st</sup> World Landslide Forum*. Tokyo, Japan,  
1188 pp 465–468

1189 Parise, M., & Cannon, S.H. (2009). A database on post-fire erosion rates and debris flows in Mediterranean-  
1190 Basin watersheds. *EGU General Assembly, Abstracts*, p. 1530.

1191 Parise, M., & Cannon, S.H. (2012) Wildfire impacts on the processes that generate debris flows in burned  
1192 watersheds *Nat Hazards* 61:217-227 doi:10.1007/s11069-011-9769-9

1193 Park, D.W., Lee, S.R., Vasu, N.N., Kang, S.H., Park, J.Y. (2016) Coupled model for simulation of landslides  
1194 and debris flows at local scale *Nat Hazards* 81:1653-1682 doi:10.1007/s11069-016-2150-2

1195 Polade, S.D., Gershunov, A., Cayan, D.R., Dettinger, M.D., & Pierce, D.W. (2017) Precipitation in a warming  
1196 world: Assessing projected hydro-climate changes in California and other Mediterranean climate  
1197 regions *Scientific Reports* 7:10783 doi:10.1038/s41598-017-11285-y

1198 Qi, Y., Martinaitis, S., Zhang, J., & Cocks, S. (2016). A real-time automated quality control of hourly rain gauge  
1199 data based on multiple sensors in MRMS system. *J. Hydrometeor.*, 17, 1675–1691,  
1200 <https://doi.org/10.1175/JHM-D-15-0188.1>.

1201 Raia, S., Alvioli, M., Rossi, M., Baum, R. L., Godt, J.W., Guzzetti, F. (2014) Improving predictive power of  
1202 physically based rainfall-induced shallow landslide models: a probabilistic approach *Geosci Model Dev*  
1203 7:495-514 doi:10.5194/gmd-7-495-2014

1204 Regmi, N.R., Giardino, J.R., Vitek, J.D. (2010) Modeling susceptibility to landslides using the weight of  
1205 evidence approach: Western Colorado, USA *Geomorphology* 115:172-187  
1206 doi:<https://doi.org/10.1016/j.geomorph.2009.10.002>

1207 Reichenbach, P., Rossi, M., Malamud, B.D., Mihir, M., Guzzetti, F. (2018) A review of statistically-based  
1208 landslide susceptibility models *Earth-Science Reviews* 180:60-91  
1209 doi:<https://doi.org/10.1016/j.earscirev.2018.03.001>

1210 Rengers, F.K., McGuire, L.A., Kean, J.W., Staley, D.M., & Hobley, D.E.J. (2016). Model simulations of flood  
1211 and debris flow timing in steep catchments after wildfire. *Water Resources Research*, 52(8), 6041-6061.  
1212 doi:<https://doi.org/10.1002/2015WR018176>

1213 Reneau, S.L., Katzman, D., Kuyumjian, G.A., Lavine, A., & Malmon, D.V. (2007). Sediment delivery after a  
1214 wildfire. *Geology*, 35(2), 151-154. doi:10.1130/G23288A.1

1215 Reynolds, C., (2021). Highway 1 washout near Big Sur expected to be fixed by summer, *Los Angeles Times*.  
1216 [https://www.latimes.com/travel/story/2021-02-25/highway-1-to-big-sur-will-reopen-by-summer-](https://www.latimes.com/travel/story/2021-02-25/highway-1-to-big-sur-will-reopen-by-summer-caltrans-says)  
1217 [caltrans-says](https://www.latimes.com/travel/story/2021-02-25/highway-1-to-big-sur-will-reopen-by-summer-caltrans-says)

1218 Robichaud, P., Beyers, J., & Neary, D. (2000). Evaluating the effectiveness of postfire rehabilitation treatments.

1219 Rosso, R., Rulli, M.C., Bocchiola, D. (2007) Transient catchment hydrology after wildfires in a Mediterranean  
1220 basin: runoff, sediment and woody debris *Hydrol Earth Syst Sci* 11:125-140 doi:10.5194/hess-11-125-  
1221 2007

1222 Rulli, M.C., & Rosso, R. (2007). Hydrologic response of upland catchments to wildfires. *Advances in Water*  
1223 *Resources*, 30(10), 2072-2086. doi:<https://doi.org/10.1016/j.advwatres.2006.10.012>

1224 Santi, P.M., deWolfe, V.G., Higgins, J.D., Cannon, S.H., & Gartner, J.E. (2008). Sources of debris flow material  
1225 in burned areas. *Geomorphology*, 96(3-4), 310-321. doi:10.1016/j.geomorph.2007.02.022

1226 Santi, P.M., & Morandi, L. (2013). Comparison of debris flow volumes from burned and unburned areas.  
1227 Landslides, 10(6), 757-769.

1228 Schaefli, B., & Gupta, H. V. (2007). Do Nash values have value? Hydrological Processes, 21(15), 2075-2080.  
1229 <https://doi.org/10.1002/hyp.6825>

1230 Scheip, C.M., & Wegmann, K.W. (2021). HazMapper: A global open-source natural hazard mapping application  
1231 in Google Earth Engine. Natural Hazards and Earth System Sciences, 21(5), 1495-1511.

1232 Schönfelder, L. H., Bakken, T. H., Alfredsen, K., & Adera, A. G. (2017). Application of HYPE in Norway.  
1233 SINTEF Energi. Rapport.

1234 Scott, D. F., & Van Wyk, D. B. (1990). The effects of wildfire on soil wettability and hydrological behaviour of  
1235 an afforested catchment. 121, 239. doi:10.1016/0022-1694(90)90234-o

1236 Scott, D. F. (1993). The hydrological effects of fire in South African mountain catchments. Journal of hydrology,  
1237 150(2-4), 409-432.

1238 Shakesby, R. A., & Doerr, S. H. (2006). Wildfire as a hydrological and geomorphological agent. Earth-Science  
1239 Reviews, 74(3), 269-307. doi:<https://doi.org/10.1016/j.earscirev.2005.10.006>

1240 Shen H., Lynch, B., Poulsen, C.J., & Yanites, B.J. (2021) A modeling framework (WRF-Landlab) for simulating  
1241 orogen-scale climate-erosion coupling Computers & Geosciences 146:104625  
1242 doi:<https://doi.org/10.1016/j.cageo.2020.104625>

1243 Sidman, G., Guertin, D., Goodrich, D., Unkrich, C., & Burns, I. (2016). Risk assessment of post-wildfire  
1244 hydrological response in semiarid basins: the effects of varying rainfall representations in the  
1245 KINEROS2/AGWA model. International Journal of Wildland Fire, 25, 268-278. doi:10.1071/WF14071

1246 Staley, D. M., Negri, J. A., Kean, J. W., Laber, J. L., Tillery, A. C., & Youberg, A. M. (2016). Updated logistic  
1247 regression equations for the calculation of postfire debris flow likelihood in the western United States  
1248 (2016-1106). Retrieved from Reston, VA: <http://pubs.er.usgs.gov/publication/ofr20161106>

1249 Staley, D.M., Negri, J.A., Kean, J.W., Laber, J.L., Tillery, A.C., & Youberg, A. M. (2017) Prediction of spatially  
1250 explicit rainfall intensity–duration thresholds for post-fire debris-flow generation in the western United  
1251 States Geomorphology 278:149-162 doi:<https://doi.org/10.1016/j.geomorph.2016.10.019>

1252 Stoof, C.R., Vervoort, R.W., Iwema, J., van den Elsen, E., Ferreira, A.J.D., & Ritsema, C.J. (2012). Hydrological  
1253 response of a small catchment burned by experimental fire. Hydrol. Earth Syst. Sci., 16(2), 267-285.  
1254 doi:10.5194/hess-16-267-2012

1255 Swain, D.L., Langenbrunner, B., Neelin, J.D., & Hall, A. (2018) Increasing precipitation volatility in twenty-  
1256 first-century California. Nature Climate Change. 8:427-433 doi:10.1038/s41558-018-0140-y

1257 Swain, D.L. (2021). A Shorter, Sharper Rainy Season Amplifies California Wildfire Risk. Geophysical Research  
1258 Letters, 48(5), e2021GL092843. doi:<https://doi.org/10.1029/2021GL092843>

1259 Tang, H., McGuire, L. A., Rengers, F. K., Kean, J. W., Staley, D. M., & Smith, J. B. (2019). Developing and  
1260 testing physically based triggering thresholds for runoff-generated debris flows. Geophysical Research  
1261 Letters, 46, 8830– 8839. <https://doi.org/10.1029/2019GL083623>

1262 Tognacca, C., Bezzola, G.R., & Minor, H.E. (2000). Threshold criterion for debris-flow initiation due to channel-  
1263 bed failure. Debris-flow hazards mitigation: Mechanics, prediction and assessment (pp. 89-97).

1264 U.S. Forest Service, Burned Area Emergency Response, Dolan Postfire BAER Soil Burn Severity Map Released,  
1265 October 10, 2020, [https://inciweb.nwcg.gov/photos/CALPF/2020-10-06-1821-Dolan-PostFire-  
1266 BAER/related\\_files/pict20200910-143346-0.pdf](https://inciweb.nwcg.gov/photos/CALPF/2020-10-06-1821-Dolan-PostFire-BAER/related_files/pict20200910-143346-0.pdf)

1267 U.S. Forest Service, Burned Area Emergency Response, Dolan Fire Burned Area Report, October 13, 2020,  
1268 [https://inciweb.nwcg.gov/photos/CALPF/2020-10-06-1821-Dolan-PostFire-  
1269 BAER/related\\_files/pict20200927-132609-0.pdf](https://inciweb.nwcg.gov/photos/CALPF/2020-10-06-1821-Dolan-PostFire-BAER/related_files/pict20200927-132609-0.pdf)

1270 U.S. Geological Survey, Postfire Debris flow Hazards: Dolan Fire (Los Padres National Forest, CA), Landslide  
1271 Hazards Program, retrieved September 27, 2021, from  
1272 [https://landslides.usgs.gov/hazards/postfire\\_debrisflow/detail.php?objectid=312](https://landslides.usgs.gov/hazards/postfire_debrisflow/detail.php?objectid=312)

1273 Vergopolan, N., Chaney, N.W., Beck, H.E., Pan, M., Sheffield, J., Chan, S., & Wood, E.F. (2020). Combining  
1274 hyper-resolution land surface modeling with SMAP brightness temperatures to obtain 30-m soil  
1275 moisture estimates. *Remote Sensing of Environment*, 242, 111740.  
1276 doi:<https://doi.org/10.1016/j.rse.2020.111740>

1277 Wang, J., Wang, C., Rao, V., Orr, A., Yan, E., & Kotamarthi, R. (2019). A parallel workflow implementation  
1278 for PEST version 13.6 in high-performance computing for WRF-Hydro version 5.0: a case study over  
1279 the midwestern United States. *Geoscientific Model Development*, 12(8), 3523-3539. doi:10.5194/gmd-  
1280 12-3523-2019

1281 Williams, A.P., Abatzoglou, J.T., Gershunov, A., Guzman-Morales, J., Bishop, D.A., Balch, J.K., & Lettenmaier,  
1282 D.P. (2019). Observed Impacts of Anthropogenic Climate Change on Wildfire in California. *Earth's*  
1283 *Future*, 7(8), 892-910. doi:<https://doi.org/10.1029/2019EF001210>

1284 Williams, A.P. et al. (2022) Growing impact of wildfire on western US water supply. 119:e2114069119  
1285 doi:10.1073/pnas.2114069119 %J Proceedings of the National Academy of Sciences

1286 Xia, Y., Mitchell, K., Ek, M., Cosgrove, B., Sheffield, J., Luo, L., . . . Lohmann, D. (2012). Continental-scale  
1287 water and energy flux analysis and validation for North American Land Data Assimilation System  
1288 project phase 2 (NLDAS-2): 2. Validation of model-simulated streamflow. *Journal of Geophysical*  
1289 *Research: Atmospheres*, 117(D3). doi:<https://doi.org/10.1029/2011JD016051>

1290 Yin D., Xue Z. G., Gochis D. J., Yu W., Morales M., & Rafieeiniasab A. (2020) A Process-Based, Fully  
1291 Distributed Soil Erosion and Sediment Transport Model for WRF-Hydro 12:1840

1292 Zhang, J. et al. (2011). National Mosaic and Multi-Sensor QPE (NMQ) system: Description, results, and future  
1293 plans. *Bull. Amer. Meteor. Soc.*, 92, 1321–1338, <https://doi.org/10.1175/2011BAMS-D-11-00047.1>.

1294 Zhang, J., Qi, Y., Langston, C., Kaney, B., & Howard, K. (2014). A real-time algorithm for merging radar QPEs  
1295 with rain gauge observations and orographic precipitation climatology. *J. Hydrometeor.*, 15, 1794–1809,  
1296 <https://doi.org/10.1175/JHM-D-13-0163.1>.

1297 Zhang, J. et al. (2016). Multi-Radar Multi-Sensor (MRMS) quantitative precipitation estimation: Initial  
1298 operating capabilities. *Bull. Amer. Meteor. Soc.*, 97, 621–638, <https://doi.org/10.1175/BAMS-D-14-00174.1>.

1300 Zhang S., Zhao, L., Delgado-Tellez, R., Bao, H. (2018) A physics-based probabilistic forecasting model for  
1301 rainfall-induced shallow landslides at regional scale *Nat Hazards Earth Syst Sci* 18:969-982  
1302 doi:10.5194/nhess-18-969-2018

1303

1304